Chapter 4
Computational Models of Vascular Mechanics

Joseph R. Leach, Mohammad R. Kaazempur Mofrad, and David Saloner

Abstract Many of the world's leading causes of death involve pathology of the vasculature, both arterial and venous. In addition to the biochemical and genetic factors governing vascular health and disease, mechanics strongly modulates the form and function of the vessel wall. Biomechanical analysis is being increasingly used to not only elucidate key disease processes, but also to predict disease progression and response to therapeutic and surgical intervention on a patient-specific basis. This chapter reviews some of the recent advances in computational vascular mechanics, with references to key works in constitutive modeling, fluid-structure interaction, image-based modeling, and atherosclerotic plaque mechanics.

Keywords Vascular · Carotid · Fluid-structure interaction · Constitutive modeling · Plaque rupture

1 Introduction

Cardiovascular pathologies including coronary heart disease, cerebrovascular disorders, peripheral arterial disease, hypertension, and congenital heart disease are the leading cause of death worldwide [1]. A substantial portion of these conditions involves pathology of the vasculature, both arterial and venous. For many vascular diseases, mechanical analyses have been shown to provide an improved understanding of disease initiation and progression, as well as the effects of surgical

J.R. Leach (✉) and D. Saloner
Joint Graduate Group in Bioengineering, University of California, Berkeley
and University of California, San Francisco
Department of Radiology, University of California, San Francisco, 505 Parnassus Ave,
San Francisco, CA 94143
e-mail: joseph.leach@ucsf.edu; saloner@radiology.ucsf.edu

M.R.K. Mofrad
Joint Graduate Group in Bioengineering, University of California, Berkeley
and University of California, San Francisco
e-mail: mofrad@berkeley.edu

and pharmacological interventions [2]. The progressing understanding of cellular mechanotransduction, and its translation to the tissue-level biological response leaves little doubt that a thorough knowledge of the stresses and strains within the vessel wall is needed.

Over the past decade, the level of sophistication with which vascular mechanics analyses can be made has increased dramatically. This is due, in no small part, to advances in computational resources and computational methods. Characterization of arterial solid mechanics behavior, with more complete and realistic constitutive relations, has been another factor allowing continued progress in the field. Additionally, advancements in medical imaging technology have allowed patient-specific studies by providing the morphological, compositional, and physiological data upon which such analyses are constructed.

The field of vascular mechanics is as branching as the vasculature itself, with current efforts in constitutive modeling, fluid dynamics, computation, medical imaging, image processing, and biochemical/biomechanical growth and remodeling simulation. This chapter serves to provide a review of recent advances in these and other sub-fields of vascular mechanics. A brief review of healthy and diseased vascular anatomy will also be presented.

2 Healthy Vessels

Although the ultimate goal of vascular mechanics analyses is often a deeper understanding of pathology, it is imperative to first understand the structure of healthy vessels. The vasculature comprises the arterial and venous vessels, which convey blood away from and toward the heart, respectively. This review will focus solely on arterial mechanics, as comparatively little work is being done in the venous realm.

The arterial vasculature consists of the pulmonary arterial system and the systemic arteries. The two pulmonary arteries arise from the pulmonary trunk to convey deoxygenated blood from the right ventricle of the heart into a tree-like structure of smaller arterioles that feeds into an even smaller system of pulmonary capillaries. The pulmonary capillaries allow gaseous diffusion to occur between the blood and the atmosphere, and the now oxygenated blood is returned to the left atrium of the heart through venules and the pulmonary veins.

The systemic arteries convey oxygenated blood from the left ventricle of the heart to the rest of the body. The aorta is the largest systemic artery (lumen diameter $\sim$2.5 cm), and receives blood directly from the left ventricle through the aortic valve. From the aorta, oxygenated blood passes to the other conducting arteries (diameter $\sim$2.5 cm–1 cm), which convey blood to the various anatomical regions. Next, blood is distributed through a branching series of tapering vessels (diameter $\sim$1 cm–300 μm) until it reaches the arterioles (diameter $\sim$300 μm–10 μm) and capillary beds (diameter $\sim$8–10 μm), where the blood exchanges gases, nutrients, and wastes with the body. In this way, the arterial vasculature is conveniently divided into four classes of vessels: conducting vessels like the aorta, distributing vessels that deliver

blood to specific organs, arterioles, and capillaries. The structure of the healthy arterial wall differs between vessel classes, reflecting their different locations in the circulatory system, and their different roles. The investigations typically made in the cardiovascular mechanics community concern the conducting and distributing vessels, and thus the arterioles and capillaries will not be considered here. A vast amount of work being done on cerebral and abdominal aortic aneurysms is primarily focused on the fluid mechanics involved. Modeling of these conditions will be discussed extensively in chapter 5, and will not be considered specifically here. The methods used in modeling these conditions from a solid mechanics perspective are the same as those discussed throughout this chapter, and most current efforts are geared toward establishing accurate constitutive relations.

2.1   Conducting Arteries

Conducting arteries are named for their function within the body, namely, conducting blood from the heart to the rest of the body. Conducting arteries are also referred to as *elastic* arteries. The aorta and other conducting vessels are generally of larger diameter ($\sim$1–2.5 cm), are thick walled, and are elastic. These bulk properties, and the underlying microstructure of the conducting vessel wall are optimized for proximity to the heart and the support of large volume flow rateces. The conducting vessel wall consists of three primary layers, the tunica intima, tunica media, and the tunica adventitia (see Fig. 1).

The intima is the innermost layer, and comprises a monolayer of biologically active endothelial cells supported by the basal lamina, which consists largely of a mesh of type IV collagen, and the glycoproteins laminin and fibronectin. The endothelium of the intima provides a non-thrombogenic interface between the vessel wall and flowing blood. All four arterial classes possess a tunica intima.
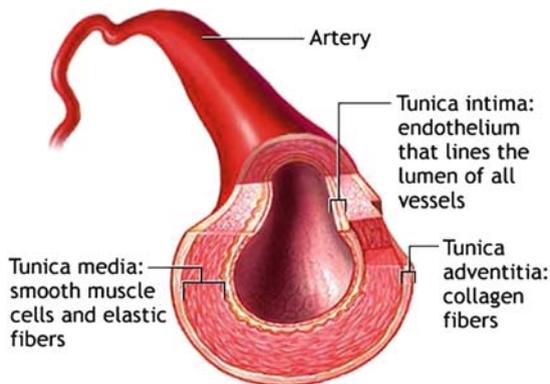
Fig. 1 Cross section of a typical conducting artery showing the intimal, medial, and adventitial layers (From http://adam.com)

Beyond the intima is the media, which is composed primarily of smooth muscle cells, elastic connective tissue, and various types of collagen. Fenestrated elastin sheets divide the media into concentric layers of smooth muscle reinforced with elastin and collagen fibrils. The innermost and outermost elastin sheets are called the inner elastic lamina and the outer elastic lamina, and they separate the media from the intima and adventitia, respectively. The smooth muscle cells and bundles of collagen fibrils of the media are often oriented helically about the vessel axis with a small pitch such that the dominant mechanical reinforcement is nearly circumferential. Vessels closer to the heart generally have a greater number of elastic lamina than more peripheral vessels, which are more muscular in structure.

The elastic compliance of the conducting vessels, and particularly the aorta, serves to smooth out the pressure wave of the cardiac cycle. When the left ventricle contracts, blood is expelled into the aorta. This sudden rise in aortic pressure, to 100–160 mm Hg, causes the vessel to distend radially, acting as a capacitor for blood. After this systolic peak, when no blood is being pushed into systemic circulation by the heart, the compliant aorta relaxes and its elastic potential energy is used to propel blood forward into the vasculature. In this way, systemic flow is maintained during diastole, and the blood flow waveform of the cardiac cycle is smoother than the pump action of the heart. The media is the most mechanically relevant layer in the healthy arterial wall, and is what gives conducting vessels their capacitance.

Outward from the media, beyond the outer elastic lamina, is the tunica adventitia. The adventitia is composed primarily of fibroblasts, ground substance, and bundles of collagen fibers. The collagen fibers are arranged roughly helically with the vessel axis. The average pitch of the helices is typically much greater than that of the medial collagen, although significant directional dispersion is often present [3, 4]. The adventitia secures the vessel to perivascular tissue and also contains the *vasa vasorum*, microvasculature that provides circulatory support to the adventitia and outer portion of the media. At low luminal pressures, the collagen fibrils in the adventitia are only partially stretched, and the adventitia is much more compliant than the media. However, under a high-pressure load, the collagen fibrils are further extended and the adventitia stiffens significantly. Thus, the structural mechanical role of the adventitia is to act as a sheath that prevents overstretching of the vessel wall. There is also nervous tissue in the adventitia, and recent studies show that this layer plays a role in growth and remodeling and maintenance of vessel tone [5, 6].

2.2 Distributing Arteries

The distributing arteries are also known as *muscular arteries*, because their thick media are made up almost entirely from smooth muscle cells. These arteries are smaller than the conducting arteries, with diameters in the range of about 1 cm to 500 µm. In the largest of the distributing arteries, there may be 30 or more layers of smooth muscle cells, and only two layers in the smallest muscular arteries. The

smooth muscle cells are circumferentially oriented, and their behavior is regulated by several different vasoactive substances [7, 8]. The vasodilatation and vasoconstriction mediated by these agents, and also by the autonomic nervous system, are a primary mechanism by which smaller distributing arteries and arterioles help regulate systemic blood pressure. The activity of the smooth muscle in these vessels also helps control the distribution of blood flow to the capillary beds of various organs and tissues [8, 9].

The media of the distributing arteries typically has very little elastin compared to the media of the conducting arteries. Often, the only elastic laminae present are the internal and external elastic lamina, which separate the media from the intima and adventitia, respectively. The proportion of collagen fibrils in the distributing vessel media is also smaller than that of the conducting vessels. The intima of the distributing arteries is compositionally similar to that of the conducting arteries but generally contains less subendothelial basal lamina tissue. The adventitia is similar to that of the conducting arteries.

For a more comprehensive review of vascular anatomy and physiology, see [2, 8, 9].

3 Healthy Arterial Mechanical Response and Constitutive Relations

For any biomechanical investigation, the character of a disease state is most fully understood when we are able to accurately compare and contrast it to the normal, homeostatic state. Thus, although many investigations in arterial mechanics are motivated to understand pathologic conditions such as hypertension, atherosclerosis, and aneurysmal disease, a careful study must also be made of the mechanics of the healthy artery under normal physiologic conditions.

Much of the early vascular mechanics work relied on analytic solutions to the governing partial differential equations. This necessitated many simplifications of the geometries, boundary conditions, and also the constitutive relations employed. With the continuing development of finite element methods and digital computers, numerical methods are used to consider more realistic conditions, and models are no longer bound to constitutive relations chosen for their ease of analytic computation. A great majority of the recent arterial mechanics research uses more advanced nonlinear constitutive relations to represent the arterial wall tissues, and the governing equations are solved on complicated domains using finite element methods almost exclusively.

Earlier work in arterial mechanics was aimed at understanding wave propagation in conducting arteries. A detailed, structure-based material representation of the arterial wall was therefore not needed; only the bulk response of the artery was of concern. The studies by Womersley [10–13] and Morgan and Kiely [14] represented the right cylindrical artery wall using simple linear thin-shell theory. Other early work in vascular mechanics saw the application of thin and thick-shell theory,

isotropic and orthotropic material formulations, vessel tethering represented as a perivascular pressure or an "inertial" Kelvin-Voight surrounding material [15], and the inclusion of initial stresses. It should be noted that the initial stresses considered by Atabek and Lew [16] were included as independent parameters to account for the effects of *in vivo* axial stretch and systemic pressurization, which are large-deformation processes that could not be accounted for in their linear elastic model. These initial stresses are not to be confused with the now well-known and often-considered *residual stresses* first acknowledged by Vaishnav and Vossoughi [17] and Chuong and Fung [18].

The healthy arterial wall is a nearly circular cylinder comprising three layers. Two of the layers, the media and adventitia, are mechanically relevant. Surgical and *post mortem* observations show that the artery is longitudinally stretched *in vivo*; severing the artery transversely causes recoil of the artery along its axis [19]. As first observed by Bergel [20], an artery cut longitudinally will spring open, forming an open sector defined by opening angle θ. Vaishnav and Vossoughi [17] and Chuong and Fung [18] noted that this indicated residual circumferential stresses in the artery wall. Residual stresses serve to reduce the maximum circumferential stresses in the wall, and also decrease the stress gradient through the wall, as shown in Fig. 2.

These residual stresses have been attributed to a differential growth process at work during development, although understanding is still limited. Simple cyclic inflation tests like those performed in [22–24] show that the typical conducting
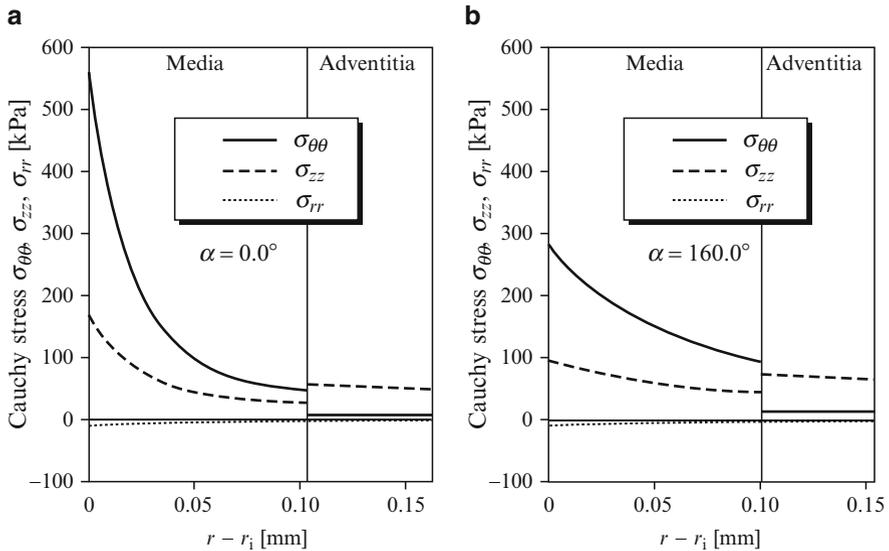
Fig. 2 Principal Cauchy stresses in the deformed media and adventitia in a physiological state (**a**) without consideration of residual stresses; (**b**) accounting for residual circumferential stresses. α denotes the opening angle of the stress-free state. These results were obtained using the constitutive relation given in Eqs. (24a, b), with the material and structural parameters listed in Fig. 3 (Taken from Holzapfel et al. [21])

artery is mechanically anisotropic [25] and has a nonlinear stress-strain behavior in both the axial and circumferential directions. Arterial tissue is also known to be nearly incompressible [26], which is a macroscopic reason for the significant axial/circumferential coupling seen in the mechanical response. Of course, there are structural reasons for this coupling as well, shown in many investigations of the vessel wall's microstructure.[1] Studies like [27, 28] have also shown the arterial wall to be viscoelastic, and possible implications of this were explored in [29]. True viscoelasticity is often not modeled in the literature however, as significant preconditioning of the vessel leads to a nearly repeatable elastic or "pseudoelastic" behavior [30]. The smooth muscle tone in arteries is regulated by several vasoactive substances and also by autonomic innervation. While a fully comprehensive mathematical representation of the artery would account for smooth muscle activity, such models are very complex and experimental data is not fully available. For this reason, nearly all recent research focuses on modeling arteries in their *passive* state.[2]

The arterial wall is thus a complicated structure, and the formulation of suitable constitutive relations is a formidable task. Through careful acquisition of experimental data, and application of nonlinear solid mechanics principles, several groups have proposed material formulations that can represent various arteries under physiological conditions. The following serves to familiarize the reader with only the basics of arterial constitutive relations, providing the very fundamental mechanics and experimental approaches, some well-known and widely applied material formulations, and a view of the trends of arterial constitutive modeling. For a more complete treatment of the relevant solid mechanics, and additional details in the formulation of arterial constitutive relations, see [2, 31–33].

The earliest characterizations of conducting artery mechanics recognized that the mechanical response was nonlinear and anisotropic. Due to a lack of suitable non-linear constitutive relations, and for ease of understanding and computation, however, early work treated arterial tissue as being linear about some reference configuration. In this way, computations of the stresses and strains in the artery wall could be made using small deformation assumptions and therefore linear formulations of stress and strain. Hayashi et al. [23] used a linear model to characterize the mechanical properties of human intracranial and extracranial arteries obtained *post mortem*. They also studied wall thickness and the thickness to radius ratio so that mechanical aspects of the origination of cerebrovascular disorders could be better understood. In their tests, freshly resected arterial segments were canulated in a physiological bath of Krebs-Ringer solution. The segments were stretched to *in vivo* length and pressurized using the bath solution so that a series of internal pressure-external radius measurements could be made. Before reliable measurements were attempted, the arterial segment was preconditioned so that stress relaxation effects were minimized. The segments were then pressurized in a consistent manner from

---

[1] See the many great references [3].

[2] See the "Current Developments" section at this chapter's end for references to the most recent fluid-solid-growth models that incorporate active vessel response and remodeling.

0–200 mmHg and pressure (P) – external radius (R_o) measurements were recorded. Hayashi et al reported their finding in terms of two parameters, the *stiffness parameter* β and the *incremental modulus* E_{inc}, given below, which describe the comprehensive stiffness of the artery segment, and the material of the arterial wall, respectively.

$$\ln\left(P/P_S\right) = \beta\left(R/R_S - 1\right) \quad E_{Inc} = \frac{\partial P}{\partial R}\frac{2(1-\nu^2)R_i^2 R_o}{(R_o^2 - R_i^2)} \tag{1a, b}$$

where P_S is the internal pressure at the reference configuration, and R_S is the reference inner radius.

The calculation of E_{inc} at the reference configuration, a transmural pressure of 100 mmHg in [23], relied on careful measurement of the internal and external radius of the segment, as well as an assumption of the Poisson's ratio ν. β and E_{inc} allowed a quantification of the material properties of intra- and extracranial arteries, and a greater understanding of the dependence of mechanical response on anatomical location and age. Such information and the similar linear characterizations made by others [34–36] were of limited value, however, in accurately calculating stress fields in materials that were known to undergo large deformations. The incremental modulus can only be used for predicting behavior of vessels in configurations very similar to the reference state. Additionally, incorporation of known residual strains is not feasible in these models due to the large deformation required in transition from a zero stress state to the residually stressed no-load state, as in [37].

Chuong and Fung stepped beyond the linear regime and used an exponential strain energy density function to describe the nonlinear mechanical response of the rabbit carotid artery [18].This allowed treatment of the arterial wall as a true three-dimensional, orthotropic, isothermal, hyperelastic solid capable of large deformations and non-linear response. The notion of pseudoelasticity was introduced by Fung [30] to address the nearly repeatable behavior of the preconditioned viscoelastic material, which could be described by separate elastic constitutive relations in loading and unloading. However, very few studies address pseudoelasticity and instead derive material constants from loading experiments only, treating the vessel wall as fully elastic. Chuong and Fung's exponential form, given below, is one of the most utilized phenomenological constitutive relations in arterial mechanics.

$$W = \frac{1}{2}c\left(e^Q - 1\right) \tag{2}$$

$$Q = c_1 E_{RR}^2 + c_2 E_{\theta\theta}^2 + c_3 E_{ZZ}^2 + 2c_4 E_{RR}E_{\theta\theta}$$
$$+ 2c_5 E_{\theta\theta}E_{ZZ} + 2c_6 E_{ZZ}E_{RR} \tag{3}$$

In the above, W is the strain energy density, c has units of stress, c_i are dimensionless material constants, and E_{jj} are components of the Green-Lagrange strain tensor

$$E = \frac{1}{2}\left(F^T \bullet F - I\right) \tag{4}$$

where F is the deformation gradient tensor and I is the second order identity tensor. The second Piola-Kirchoff stress tensor is given by

$$S = \frac{\partial W}{\partial E} \tag{5}$$

and can be transformed to recover the Cauchy stress tensor as

$$\sigma = J^{-1} F \cdot \frac{\partial W}{\partial E} \cdot F^T \tag{6}$$

where $J = \det F$ is the local volume ratio in the deformed state. A common approach that addresses incompressibility constraints and is better suited for use in computational mechanics decouples the strain energy density function into a volume-changing component and an isochoric component. This allows the Cauchy stress to be written as

$$\sigma = -pI + F \cdot \frac{\partial W}{\partial E} \cdot F^T \tag{7}$$

where p is a Lagrange multiplier which enforces incompressibility.

Whereas the second Piola-Kirchoff stress is convenient for theoretical consideration of nonlinear mechanics, the Cauchy stress is preferred in experiment because it describes the stress field within the solid in the deformed state. Because of this, the Cauchy stresses can be utilized in the determination of the material constants c_i of Eq. (3).

To specify the dimensionless material parameters c_i, a specimen is generally subjected to a known load and allowed to reach equilibrium (other studies can address creep and relaxation). The equilibrium balance equations, with the applied load boundary conditions reveal the magnitudes of the relevant Cauchy stresses, and the stretches or strains are measured experimentally. The model representation of the Cauchy stresses, dependent on c_i, are equated to the stresses determined from the equilibrium condition, and the c_i are solved for. Practically, for three dimensional states of deformation, this is done for several loading boundary conditions and the c_i are determined through a nonlinear least-squares optimization.

Although the original form of Eq. (3) did not contain shear terms, they are easily included to account for more general kinematics, and this has been done in [33]. Chuong and Fung used Eqs. (2) and (3) to describe well the non-linear orthotropic behavior of canine carotid arteries under non-shearing loads. Indeed, the success of this constitutive model is evidenced by its frequent use in the literature [33, 38–41].

Others have proposed phenomenological constitutive relations for the arterial wall that rely on functional behaviors other than exponential. Vorp et al. [42] assumed no particular form for the Hyperelastic strain energy density function used to model canine carotid arteries and rabbit aortas, but instead assumed that it was smooth enough to be represented as the Taylor series expansion

$$W = A_1 E_{11} + A_2 E_{22} + A_3 E_{33} + A_4 E_{12}^2 + A_5 E_{13}^2$$
$$+ A_6 E_{23}^2 + A_7 E_{11}^2 + A_8 E_{22}^2 + A_9 E_{33}^2$$
$$+ A_{10} E_{11} E_{22} + A_{11} E_{11} E_{33} + A_{12} E_{22} E_{33} \qquad (8)$$
$$+ \frac{\kappa}{2} (I_3 - 1) + O(E^3)$$

where $I_3 = \det(\boldsymbol{F})^2$ is the third invariant of the right Cauchy-Green tensor. In this way, W takes on a polynomial characteristic, with material parameters A_i, A_{ij}, and κ being equivalent to the Taylor series partial derivatives. Vorp et al used Eq. (8) to model arterial tissue as an orthotropic, isothermal, hyperelastic material. It should be noted that they chose to model the tissue as compressible, noting Chuong and Fung's [43] observation that arterial fluid extrusion through the vessel wall leads to *slight compressibility.* Viscoelastic effects and residual stresses were neglected in the paper, as the focus was determining constants A_i, A_{ij}, and κ through a nonlinear regression of experimental data against the Cauchy stresses derived from Eq. (8). Vorp et al. used unpublished data from Brant's experiments, as described in [35], and from Humphrey's experiments as described in [44], to this end. Both experimental setups were well validated, and the unloaded *ex-vivo* configuration of the arterial segments was used as a reference state. A finite element representation of the arterial segments was subjected to the experimental loading conditions and a displacement field was solved using FEM analysis. A dynamic simulation, rather than a static model, was made that would approach experimental loading conditions in the large-time limit; this was done for reasons of reduced computational memory requirements. The constants A_i, A_{ij}, and κ were determined through a least-squares minimization of the disagreement between the experimental displacement field and that predicted by the FEM analysis. Initially, estimates of the constants were used to define the FEM model, and regression was performed iteratively using Levenberg-Marquardt type steps to determine improved estimates of the constants. Figures 4 and 5 in [42] demonstrate the ability of Vorp et al's technique to characterize the canine and rabbit arterial responses.

Combined finite element – optimization techniques have been used successfully in the biomechanics community for characterization of many tissues, including myocardium [45] and heart valves [46]. *In vivo* and *in vitro* imaging can provide information about the strain states naturally encountered by the tissue, and thus data to which a theoretical model may be fit, as in [40]. Many techniques for the optimization of material parameters exist, including least-squares fitting and response surface methods. The details of these methods are beyond the focus of this chapter, and the interested reader is referred to the literature.

Several adaptations of the generalized Mooney-Rivlin constitutive relation have been used to represent the response of carotid and coronary arteries. In its generalized form, the strain energy density is given by Bathe [47] as

$$W = C_1(I_1 - 3) + C_2(I_2 - 3) + C_3(I_1 - 3)^2 + C_4(I_1 - 3)(I_2 - 3)$$
$$+ C_5(I_5 - 3)^2 + C_6(I_1 - 3)^3 + C_7(I_1 - 3)^2(I_2 - 3)$$
$$+ C_8(I_1 - 3)(I_2 - 3)^2 + C_9(I_2 - 3)^3 + D_1(e^{D_2(I_1 - 3)} - 1) \qquad (9)$$

where the C_i and D_1 are constants having units of stress, D_2 is a dimensionless material parameter, and I_1, I_2, and I_3 are the first, second and third invariants of the right Cauchy-Green tensor.

Delfino [19] used a truncated form of Eq. 9 first presented by Demiray [48] to model the human carotid bifurcation. In this implementation, $C_i = 0$ for $i = 1$–9, and $D_1 = a/b$, $D_2 = b/2$, where a and b are material parameters to be fit to experimental data. Delfino tested seven freshly resected disease-free cadaveric common carotid artery segments, collecting pressure-internal radius and axial force-radius measurements when the cylindrical specimen was held at axial stretches of 1.05, 1.1, and 1.15. Because the specimens were different sizes, averaging was done on circumferential and axial distensibility measures $D_C(P)$ and $D_A(F)$ that accounted for non-uniform internal radii, r_i.

$$D_C(P) = \frac{1}{S}\frac{\partial S}{\partial P}$$
$$D_A(F) = \frac{1}{S}\frac{\partial S}{\partial F} \qquad \text{(10a, b, c)}$$
$$S = \pi\, r_i^2$$

After establishing average distensibilities, Eqs. 10 were integrated to determine an average pressure-radius and axial force-radius relationships for the healthy carotid artery. Delfino notes that the final material characterization yielded a strain energy density function that was polyconvex within a strain range of –0.25–36, which is important for material and mathematical stability of a constitutive relation, as non-convexity can lead to singularities and numerical error.

Tang et al have used a different truncation of the generalized Mooney-Rivlin model to represent both poly-vinyl alcohol hydrogel models of stenotic arteries and healthy and diseased human carotid arterial wall. The hydrogel is shown to be similar in response to healthy bovine carotid arteries in [49]. Tang et al used the form below and determined the material coefficients c_1, c_2, D_1, and D_2 by fitting to published experimental data [50–53].

$$W = c_1(I_1 - 3) + c_2(I_2 - 3) + D_1(e^{D_2(I_1-3)} - 1) \qquad (11)$$

Raghavan et al also used a truncation of the generalized Mooney-Rivlin constitutive relation to represent a "generic" 1-layer arterial segment in their study of residual circumferential stress [37]. In this work, the strain energy density function was given by

$$W = a(I_1 - 3) + b(I_1 - 3)^2 + c(I_1 - 3)^3 \qquad (12)$$

in which a cubic term constitutes an addition to the standard Mooney material. In order to compare their results to the published results of others, Raghavan et al determined a, b, and c by fitting to the experimental data acquired for rabbit thoracic aortas by Chuong and Fung [54]. Chuong and Fung's material model treated the artery as anisotropic, having different behavior in the radial, circumferential, and

axial directions. The Mooney-Rivlin model used by Raghavan et al is isotropic, and thus a systematic approach was made to fit theory to experiment. First, Chuong and Fung's model was reduced to an equibiaxial extension case in the θ and Z directions, and stress-strain data were generated using their material parameters. Raghavan et al's model was also reduced to an equibiaxial extension form (both θ and Z directions being equal, due to isotropy), and the material parameters for the θ and Z directions were established through fitting to the stress-strain data derived from the Chuong and Fung model. The material parameters in the θ and Z directions were then averaged to determine the representative isotropic response for the unspecified artery.

The recent literature contains several other phenomenological constitutive relations for the healthy arterial wall. Of the hyperelastic models proposed, some use strain energy functions that have polynomial forms different from those already discussed, while others use a different sub-form of the generalized Mooney-Rivlin material. Others, notably the constitutive relation proposed by Takamizawa and Hayashi [22], are based on a logarithmic form of the strain energy density function. Humphrey [2] noted that although their material model represents well the response of the canine carotid artery under certain conditions, Takamizawa and Hayashi's model is incapable of strong anisotropy and may not be easily used when shear stresses are considered. The simple Neo-Hookean formulation, which may be considered a variant of the Mooney-Rivlin formulation, has also seen abundant use and will be discussed more in the next section. At least one group [55] has employed a two-term Ogden model to represent the healthy human carotid artery.

Zhang et al [56] proposed a generalized Hooke's law to represent the arterial wall. In their model the authors employ a generalized Hencky strain tensor $\boldsymbol{D}$, specifically the logarithmic-exponential strain

$$\boldsymbol{D} = \ln(\boldsymbol{U})e^{n(I_1 - 3)} \tag{13}$$

to absorb the nonlinearity of the vascular stress-strain relation. In this definition of strain, $\boldsymbol{U}$ is the right stretch tensor that results from a decomposition of the deformation gradient into a rigid rotation and a pure stretch.

$$\boldsymbol{F} = \boldsymbol{R}\boldsymbol{U} \tag{14}$$

In this way, the authors can write the stress-strain relation for the arterial wall as a generalized three dimensional Hooke's law. Without shear:

$$\begin{pmatrix} S_{\theta\theta} \\ S_{zz} \\ S_{rr} \end{pmatrix} = \begin{pmatrix} c_{11} & c_{12} & c_{13} \\ c_{21} & c_{22} & c_{23} \\ c_{31} & c_{32} & c_{33} \end{pmatrix} \begin{pmatrix} D_{\theta\theta} \\ D_{zz} \\ D_{rr} \end{pmatrix} \tag{15}$$

This approach, although needing ten constants to be specified for a material, reduces the stress-strain relation to a linear one, and necessitates only one nonlinear term, n from Eq. (13). Although ten material parameters is more than some other very

capable constitutive relations, the linear dependence of S on all but one of these parameters allows very easy and stable linear regression methods to establish their values for a particular tissue. The authors have shown that the constitutive relation works well for modeling the response of porcine coronary arteries [57].

Phenomenological constitutive relations have been used extensively in vascular mechanics research during the past few decades. Their use has allowed the investigation and characterization of the nonlinear mechanical response of various arteries under normal and pathological conditions. Although many of these material formulations are capable of representing well the mechanical response of an artery, their (sometimes many) material parameters and fitting constants often do not have a clear physical interpretation such as Young's modulus for linear elasticity. Most recently, constitutive relations are designed with histological structure in mind. The result of such an approach is often a material formulation with fewer parameters, and a more clear physical meaning for each parameter. The structural approach also benefits from direct physical interpretation in that singular behavior and non-convexity is more easily avoided [58].

The material characterization of Wuyts et al [59] is likely the first comprehensive structural material formulation made specifically for the arterial wall. The model itself, and the studies of material properties and their dependence on anatomical location and age are an important contribution to the literature. The model of [59] contains many of the salient features of arterial mechanics, but is not easily incorporated into a computational approach, and is not easily extended to arbitrary geometries. Because the remainder of this chapter will focus on recent computational models of the vasculature, the model of Wuyts et al will not be covered further. Instead, a phenomenological model with a strong basis in the relevant nonlinear mechanics, and a clear computational efficiency, is discussed.

Perhaps the best segue from phenomenological to the most modern structural constitutive relations is the constitutive relation of Holzapfel and Weizsacker from [32]. In this paper, the authors present a relation where the strain energy function is additively split into two parts, one to account for the isotropic response and the other to account for the anisotropic response.

$$\psi = \psi_{iso} + \psi_{aniso} \qquad (16)$$

In [32] the authors state "The first term of the potential, i.e., ψ_{iso} represents the *isotropic* contribution (probably stemming from the 'elastin of the vascular wall') ... The second term, i.e., ψ_{aniso} represents the *anisotropic* contribution (likely from the 'collagen of the wall')". Thus, the constitutive relation is designed to address *actual* artery wall materials separately, albeit still using a phenomenological approach. In Holzapfel and Weizsacker's strain energy density function, the isotropic response is modeled as a Neo-Hookean material

$$\psi_{iso} = c_1 (I_1 - 3) \qquad (17)$$

and the strain-stiffening behavior of the anisotropic collagen in the wall is incorporated through a Fung exponential relation.

$$\psi_{aniso} = c_2(e^Q - 1)$$
$$Q = a_1 E_{11}^2 + a_2 E_{22}^2 + a_3 E_{33}^2 + 2a_4 E_{11} E_{22} + 2a_5 E_{22} E_{33}$$
$$+ 2a_6 E_{11} E_{33} \tag{18,19}$$

Normal physiologic loading of a straight arterial segment does not induce shear stresses, and thus Q is free of shear terms. The authors chose to treat the arterial wall as a thin membrane, and assumed the membrane was capable only of states of plane stress. Further, a two-dimensional approach was taken, with a_3, a_5, and a_6 equal to zero, and the radial strain E_3 is neglected rather than determined by incompressibility constraints. After these assumptions, Q takes the form

$$Q = a_1 E_{11}^2 + a_2 E_{22}^2 + 2a_4 E_{11} E_{22} \tag{20}$$

and represents a compressible material. Holzapfel and Weizsacker used their constitutive relation to generate models for both the rat abdominal aorta and tail artery, an elastic and muscular artery, respectively. Figures 2 and 4 in [32] demonstrate that although the five-parameter model cannot recreate all features of the stress-strain behavior of the arteries, the *biphasic* nature of the elastic aorta is captured well, and the same model is able to represent the *monophasic* behavior of the tail artery. The *biphasic* response in the circumferential direction of an elastic artery is attributed to the low-strain response of the elastin content being overcome by the exponential, strain-stiffening response of collagen content at higher strains. This feature cannot be captured by an exponential Fung model alone. The authors noted that their two-term strain energy density function is "promising in the quest of correlating arterial structure to mechanics" [32], and indeed it ushered in a new, more realistic, class of structural constitutive relations to represent the arterial wall in a manner well suited for computational analysis.

In [21], Holzapfel, Gasser, and Ogden introduced a new type of constitutive relation for the healthy arterial wall. The constitutive relation was designed and specified by considering the artery wall to be a two-layer structure, as the medial and adventitial layers are mechanically relevant (in a solids sense) in a healthy artery, but the intimal layer is not. Each layer is treated as a nonlinearly elastic, thick walled, orthotropic, incompressible, isothermal fiber reinforced material with residual strains. Incompressibility is effectively handled by decomposing the strain energy density function Ψ into a volume-changing component $U(J)$ that depends on the local volume ratio J, and an isochoric component $\bar{\Psi}$. The Cauchy stresses thus contain a $p\boldsymbol{I}$ term where p is a Lagrange multiplier that can account for the hydrostatic stress response.

As in [32], the isochoric portion of the strain energy density function of [21] for each layer is further additively split into an isotropic component and an anisotropic component. The isotropic component is used to model the non-collagenous material of the layer, while the anisotropic component models the mechanical response of the two collagen fiber families that are symmetrically disposed and helically oriented about the layer's axis.

$$\bar{\Psi}(\bar{\boldsymbol{C}}, \boldsymbol{a}_{01}, \boldsymbol{a}_{02}) = \bar{\Psi}_{iso}(\bar{\boldsymbol{C}}) + \bar{\Psi}_{aniso}(\bar{\boldsymbol{C}}, \boldsymbol{a}_{01}, \boldsymbol{a}_{02}), \tag{21}$$

where a_{01} and a_{02} are the reference direction vectors for the two fiber families in the layer. The isotropic response of each layer is modeled using the neo-Hookean strain energy density function

$$\bar{\Psi}_{iso} = \frac{c}{2}(\bar{I}_1 - 3), \tag{22}$$

where $\bar{I}_1$ is the first invariant of the "isochoric" right Cauchy-Green tensor, $\bar{C}$. The strain energy density function for the anisotropic response in each layer is given by

$$\bar{\Psi}_{aniso}(\bar{I}_4, \bar{I}_6) = \frac{k_1}{2k_2} \sum_{i=4,6} (e^{k_2(\bar{I}_i - 1)^2} - 1)$$

$$\bar{I}_4(\bar{C}, a_{01}) = \bar{C} : (a_{01} \otimes a_{01}) \tag{23a, b, c}$$

$$\bar{I}_6(\bar{C}, a_{02}) = \bar{C} : (a_{02} \otimes a_{02})$$

where k_1 has the units of stress and k_2 is a dimensionless constant. The two fiber families per layer are assumed to have the same k_1 and k_2. With respect to Fig. 3, the statement of the full constitutive problem is

$$\bar{\Psi}_M = \frac{c_M}{2}(\bar{I}_1 - 3) + \frac{k_{1M}}{2k_{2M}} \sum_{i=4,6} (e^{k_{2M}(\bar{I}_{iM} - 1)^2} - 1)$$

$$R_i \le R \le R_i + H_M$$

$$\bar{\Psi}_A = \frac{c_A}{2}(\bar{I}_1 - 3) + \frac{k_{1A}}{2k_{2A}} \sum_{i=4,6} (e^{k_{2A}(\bar{I}_{iA} - 1)^2} - 1) \tag{24a, b}$$

$$R_i + H_M \le R \le R_O$$

with the fiber direction vectors related to the fiber angles β by

$$[a_{01j}] = \begin{bmatrix} 0 \\ \cos\beta_j \\ \sin\beta_j \end{bmatrix}, \quad [a_{02j}] = \begin{bmatrix} 0 \\ \cos\beta_j \\ -\sin\beta_j \end{bmatrix}, \tag{25a, b}$$

The full details and derivation of the constitutive relation are given in [21]. The authors used rabbit carotid artery data from [30] to determine the material and structural parameters listed in Fig. 3, while the geometrical properties, referencing both the stress-free and residually strained states, are taken directly from [18]. c_A was set to one tenth c_M in keeping with the observations in the literature that the isotropic response of the media is about an order of magnitude stiffer than the adventitia. The authors note that if $\bar{I}_4$ or $\bar{I}_6$ is equal to or less than 1, that portion of the anisotropic strain energy density function is not to be incorporated in the full strain energy. This effectively accounts for the fact that collagen fibers are incapable of supporting compressive stresses. Important for numerical simulation, with compressive stresses left unsupported by the anisotropic material component, the strain energy density function is guaranteed to be convex [58].

	Material	Geometry
Media	c_M = 3.0000 [kPa] k_{1M} = 2.3632 [kPa] k_{2M} = 0.8393 [–]	H_M = 0.26 [mm] β_M = 29.0°
Adventitia	c_A = 0.3000 [kPa] k_{1A} = 0.5620 [kPa] k_{2A} = 0.7112 [–]	H_A = 0.13 [mm] β_A = 62.0°
	R_i = 0.71 [mm] for α = 0.0° Ri = 1.43 [mm] for α = 160.0°	
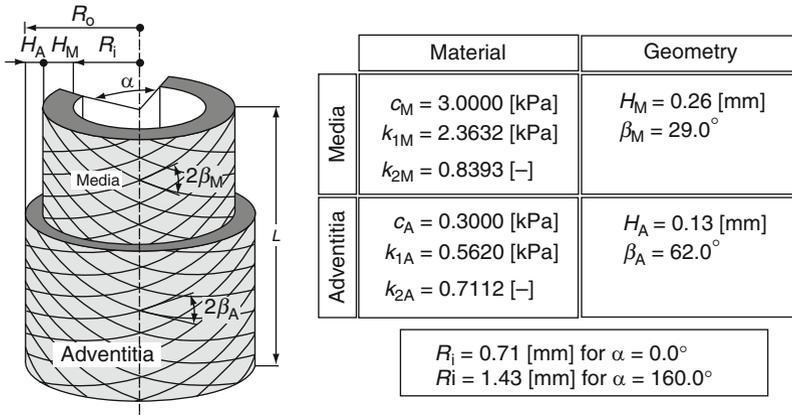
Fig. 3 Graphical representation of the two-layer arterial model considered by Holzapfel et al. [21]

The constitutive relation and comprehensive approach of [21] provided a solid and general foundation on which tremendous progress has been based. The authors of [21] used a similar approach to construct a framework for viscoelasticity in fiber-reinforced composites in [60]. Although this work focuses on the mechanics of fiber-reinforced rubber tubes, it is noted that such a formulation for viscoelasticity is easily applicable to the constitutive relation put forth for the arterial wall. In [61], Gasser and Holzapfel further extended their methods to account for elasto-plasticity in biological tissue. The authors used a multiplicative decomposition of the deformation gradient tensor into an elastic component and a plastic deformation component, in addition to a multiplicative decomposition of the deformation into spherical dilation and unimodular components. Using an elastic predictor-plastic corrector method, and a backwards Euler scheme to integrate the flow rule, the authors implemented multisurface plasticity into their fiber-reinforced composite material formulation. The utility of such a model in investigations of translumi-nal percutaneous angioplasty will be discussed in a later section of this chapter. In [62], the same authors modified the anisotropic portion of the strain energy density function from [21, 58] to accurately model human coronary arteries with non-atherosclerotic thickening of the intima. This work required the straightforward extension of their previous investigations to model the vessel wall as a three-layer fiber reinforced composite, as a thickened intima can play a large role in the vessel's mechanical response. In [3] Gasser, Ogden, and Holzapfel also extended the ma-terial formulation to account for the directional dispersion of collagen fibers in the artery wall. This is important in the intima and adventitia, where unlike the media, collagen fibers are oriented much less strictly with respect to the average direction vector. The authors used an orientation density function, incorporated as a generalized structure tensor. For the dispersion considered, the generalized structure tensor is described by a scalar dispersion parameter κ and is thus easily incorporated into a finite element approach. A transversely isotropic von Mises distribution was employed to describe the actual dispersion in each layer. The limiting cases of the

dispersion, $\kappa = 0$ and $\kappa = 1/3$ were shown to reduce to the parallel fiber [21] and isotropic (similar to [19]) constitutive relations, respectively. Kroon and Holzapfel [63] have recently extended this body of work to model $n-$layer collagenous materials. Such a model would be immensely useful in studying, among other tissues, cerebral aneurysms, where the arterial wall is often a thin, multi-layered composite of collagen "fabrics" of varying mean fiber orientation as noted in [2].

The general ideas presented in [21, 32, 41, 60, 61], among other works, have been the starting point for many additional studies into structural constitutive modeling of the arterial wall. The balance between phenomenological content and structural content varies amongst recent work, and is dictated by the study's desired level of accuracy and detail. Zulliger et al, in [64], used the idea of an additive decomposition of the strain energy density function into isotropic and anisotropic components. Their study investigated using strain energy density functions for each component, ψ_{iso} and ψ_{aniso}, that were based more completely on the histological structure of the arterial wall. The authors weighed the contributions of the isotropic and anisotropic strain energy density functions by the cross sectional area fractions of elastin and collagen, f_{elast} and f_{coll}, respectively. The nonlinearity of the isotropic strain energy density function was enhanced from that in [21] to fit experimental data, noting that while elastin may be a linearly elastic material, interaction between fibers can lead to nonlinear behavior.

$$\psi_{iso} = f_{elast}\psi_{elast} = f_{elast}c_{elast}(I_1 - 3)^{3/2} \tag{26}$$

It should be noted that Zulliger at al cited Milnor [65] in treating the elastin matrix to behave nonlinearly, while Wuyts et al [59] cite Carton [66] in treating the elastin of the media to be Hookean up to large strains. Clearly, more work needs to be done to understand the full behavior of elastin fibers and structures, and there may be no one best way to characterize the elastin content of the vessel wall.

To account for the collagen fiber content of the arterial wall, Zulliger et al noted that collagen fibers in an ensemble do not all begin to support stress at the same macroscopic strain. This is due to the non-uniform crimping and lengths of the collagen fibers in the arterial wall. The authors used an idea from earlier literature, including [59], that there exists a statistical distribution of engagement strain for the fiber ensemble. Characterizing this engagement strain distribution ρ_{fiber} as a log-logistic model, the authors used a convolution integral to relate the strain energy function of a single fiber to that of the entire ensemble in the wall tissue.

$$\psi_{coll}(\varepsilon) = \psi_{fiber}^{*}\rho_{fiber} = \int_{-\infty}^{\infty} \psi_{fiber}(x) \cdot \rho_{fiber}(\varepsilon - x)dx \tag{27}$$

The authors fit their model to experimental data from the medial layer of rat carotid arteries and compared their model predictions to those obtained using the strain energy density functions from Chuong and Fung [18], and Holzapfel et al [21]. While the predictions from the strain energy function of [18] were the best fit to the data overall, the model's predictions in strain states where collagen bears more

load are not a good fit. The strain energy density function put forth by Zulliger et al provided an overall better fit than that proposed in [21], but the predictions in the high strain region were still not entirely satisfactory. The author's choice of a log-logistic engagement strain distribution was noted to be "fairly arbitrary," as a lower bound to the distribution is the only non-statistical requirement. A different choice of distribution function and accounting for collagen fiber directional dispersion might improve the model. Recently, Roy et al [67] used a modification of the constitutive formulation from [64] as a platform to investigate the nature of elastin in the arterial wall. They found that a majority of the elastin content of the wall is in series with smooth muscle cells, the remainder acting in parallel. This is shown to have important implications on the true nature of the zero-stress state, commonly accepted as the state of an arterial segment after a radial cut. Although the paper will not be covered in detail here, the work of Ogden and Saccomandi [68] incorporates mesoscopic information on the extensibility of collagen and elastin fibers into the macroscopic constitutive relations for the arterial wall. In [68], the limiting chain extensibility of the two fiber types is incorporated using the Gent or "Fung-Demiray" (see Eq. (36)) models for the isotropic component of the strain energy density function. Adding these isotropic functions to the anisotropic Horgan-Saccomandi or Holzapfel (see Eqs. (23a, b, c)) strain energy density functions, respectively, gives two different additively split strain energy functions, as in Eq. (16), capable of representing both the arterial and rubber tube inflation-extension response. This approach affords a clear manner in which to address the quality and strain-stiffening response of fiber families, which may prove useful in more recent models that incorporate the effects of ageing and remodeling.

4 Mechanics Studies of Non-Atheromatous Arteries

The modern computational mechanics analysis of a healthy artery comprises several components. Constitutive relations, as we have seen, take on several different forms within both the phenomenological and structural frameworks. Certain relations are able to represent very accurately the distinct mechanical responses of the layers of the healthy arterial wall, while others provide a stress-strain relation that characterizes the response of the entire wall thickness in a comprehensive manner. Anisotropy, non-linearity, and viscoelasticity are addressed to varying degrees, and are incorporated in different models using different strategies. All of this has led to a wide range of material formulations in terms of accuracy, computational cost, material and mathematical stability, and applicability to complex geometries.

In addition to the constitutive relations used to represent the arterial wall, the vessel geometry, boundary conditions and loading scheme define the arterial system to be analyzed. While the mathematical techniques used in modern vascular mechanics studies are equally important to the aforementioned model parameters, a rigorous discussion is beyond the focus of this chapter, and only the major features of common approaches will be covered.

4.1 Healthy Geometry, Healthy Material

Most studies made of healthy vessels concern themselves with idealized geometries. A circularly cylindrical, non-branching segment with boundary constraints that exploit symmetry is most common in the literature, and represents portions of many healthy arteries quite well. The single- or multi-layered models of straight, non-stenotic arterial segments are most often used to develop and test constitutive relations for the artery wall. When the constitutive relation is shown to predict experimental loading and strain data with acceptable accuracy, the model can be used to quantify the stresses within the healthy arterial wall. Although the action of the heart and viscous blood flow are what impart force (besides residual stresses) on the artery wall, the pressure drop across a healthy arterial segment is normally very small, and uniform pressure loading is an often-employed and well-justified assumption in static or quasi-static analyses. The wall shear stress felt by the intimal surface of the vessel wall is certainly biologically relevant, but is orders of magnitude smaller than the stresses imparted by systemic pressure in most healthy, non-stenotic vessels. For many of these arteries, shear stresses can be predicted with reasonable accuracy using computational fluid dynamic models that do not explicitly model the mechanical response of the artery wall. More advanced methods that couple fluid and solid mechanics are possible for this calculation, and will be discussed later.

The studies referenced in the previous section of this chapter provide many fine examples of non-atheromatous arterial wall stress calculations in idealized geometries. Although many vascular mechanics studies use finite element methods to calculate stresses and strains, the studies of the previous section generally rely on analytical methods when formulating and testing constitutive relations. An excellent analytical study of healthy arterial mechanics is provided by Humphrey and Na in [33]. In that paper, the authors examine the circumferential, axial, and radial stresses in an idealized vessel segment modeled using a strain energy density function adapted from that of Chuong and Fung [18]. Material parameters were also obtained from [18], and thus the model was an idealized rabbit common carotid artery. The authors considered the effects of flow-induced wall shear stress (although not included in their final calculations), perivascular tethering, mechanical anisotropy and material nonlinearity. Additionally, the authors explored the implications of smooth muscle activation, using the approach of Rachev and Hayashi [69]. It should be noted that nearly every arterial mechanics study assumes that the vascular smooth muscle is in a fully passive state.

Aside from constitutive model design and testing, and healthy artery stress calculations, the idealized vessel segment model is employed in studies of residual stress and supraphysiologic loading. For these types of studies, finite element methods are typically employed, as geometrical and material nonlinearity are present. Raghavan et al [37] employed an idealized vessel segment model to study the effects of segment length and "circularity" on residual stress calculations. A common approach in the literature to calculate residual stresses begins with a radial cut to a vessel segment and measurement of the opening angle and inner and outer radii of the open sector. This data, combined with an assumption of constant axial stretch allows for

an analytical calculation of residual stress throughout the artery wall, as shown in [18, 54]. This method effectively calculates the stresses in the wall that result from re-joining the cut ends of the open sector. The assumption of constant axial stretch works well for experimental observation of a small central segment of a lengthy artery, but segments for which opening angle and radii data are typically collected may not be lengthy enough to justify the assumption. End effects may render the constant axial stretch assumption invalid when the specimen length is small, which would lead to distorted residual stress calculations. Raghavan et al constructed a structured finite element mesh of an idealized open sector and performed numerical experiments to determine how specimen length effected residual stress calculations. In their model, Raghavan et al discretized the open sector with eight-node hexahedral elements that use linear shape functions. The model solved for elemental stresses using a mixed finite element formulation to account for the assumption of incompressibility. The analysis showed that an experimental specimen for which residuals stresses would be analytically or numerically calculated should be at least ten times longer than the thickness of the wall to avoid end effects.

Another common assumption in the calculation of residual stresses in arterial segments is that the open sector is a portion of a circular annulus. This simple geometry allows for the easy calculation of residual stresses based on the aforementioned opening angle and radii measurements. Experimentally, the radially cut artery segments are not quite circular in nature, and thus such an assumption may distort the calculated residual stresses. Also in [37], Raghavan et al explored the implications of the "circularity" assumption by comparing the residual stresses predicted for a discretization of a real arterial segment to those predicted for an idealized, circular segment of similar dimensions. The authors built an unstructured hexahedral mesh from digitized geometrical data of a radially cut porcine femoral artery. A structured mesh was built for an idealized open sector that was designed to have the same opening angle, wall thickness, and mesh volume as the unstructured mesh, thus serving as a control. The same finite element procedure of "rejoining" the cut ends was used to calculate the residual stresses for each model. The authors reported circumferential variations in the stresses predicted for the real artery, due to non-circularity and variations in wall thickness. The "closed," residually stressed meshes were analyzed in 15° sectors after normalizing for local wall thickness. The authors found that the residual circumferential stresses for the control geometry were consistently within a standard deviation of the stresses from the real, noncircular geometry.

4.2 High Pressure Response

A severely stenotic artery might warrant transluminal percutaneous angioplasty to restore lumen patency. In angioplasty, a balloon catheter is inserted into the vessel lumen and the balloon is expanded in the location of the stenosis. Inflation of the balloon to pressures several times greater than the systemic pressure leads to a "controlled vessel injury" wherein atherosclerotic plaque materials may be redistributed

in the vessel wall, and non-diseased tissues of the wall are overstretched. The over-stretching of non-diseased arterial tissues causes an inelastic response and some portion of the deformation is non-recoverable. The damage from overstretch maintains the increased patency of the vessel, and blood flow can return to a more normal state. Holzapfel and Gasser employed their elastoplastic fiber reinforced composite material model from [61] to simulate the overstretching of a left anterior descending coronary artery due to an internal pressure load of 100 kPa, roughly eight times normal mean systemic pressure [70]. This material model is phenomenological and is based upon an idea of collagen fibers "slipping" in the matrix, and material hardening effects are considered. Geometrical and opening angle data for the media and adventitia was taken from a previous study, and was used to account for residual stresses in the two-layered model. The idealized geometry was discretized using Q1P0 eight-node hexahedra, and loading was considered to be uniform. In the study, the authors first determined the wall stresses in the no-load, residually stressed state, then calculated wall stresses at physiological (100 mmHg) and supraphysiologic loading (750 mmHg). Upon relaxation of loading from supraphysiologic to physiological levels, a permanent deformation in the tissue was apparent, and the internal radius of the vessel increased by 0.158 mm, or nearly 5%. The wall stresses at physiological pressure were shown to be significantly altered after supraphysiologic loading, and the gradient of the circumferential stress through the media reversed sign. Although angioplasty is performed on vessels of irregular shape and composition, due to atherosclerotic changes, the inelastic deformation of remaining healthy tissues is seen experimentally to be an important factor in procedure outcome. Thus, this geometrically and compositionally simple model is a sound first step toward models that address more realistic features of a diseased, stenotic artery undergoing angioplasty. Such models will be addressed in a later section of this chapter.

5 Fluid-Structure Interaction

The pressure drop across a short segment of a typical large artery (aorta, subclavian, carotid, iliac, etc.) is normally quite small, on the order of 10 Pa/cm (compared to 13,322 Pa systemic pressure) in the common carotid artery at peak systole. Thus, for a straight arterial segment of fairly constant luminal diameter, a uniform pressure load is a reasonable approximation. When the luminal diameter is focally narrowed, called stenosis, the pressure drop associated with the same flow rate can be much greater. In this case, the assumption of a uniform pressure load is often not justified, as the wall stresses of interest are often in the region where the pressure perturbation is greatest. To make an accurate analysis of wall stresses for these cases, the pressure field should be specified using either comprehensive experimental data, or information provided from a computational fluid dynamics simulation.

Obtaining an experimental mapping of arterial pressure is fraught with difficulty, as either an invasive procedure is required of the patient, or a complicated experiment is performed in which medical images of the vessel are used to create

a physical model on which pressure measurements are made. Even if either of these methods are used, a *comprehensive* mapping of the pressure field is not feasible in most interesting cases, as we know that arterial pressure is a complicated, time-dependent, three-dimensional field with sometimes-sharp spatial and temporal gradients. Additionally, although the flow-induced shear stresses are often much smaller than systemic pressures, it is impossible to capture these in a comprehensive sense as well. Such problems also arise in studies of idealized geometries. For these reasons, computational fluid dynamics (CFD) methods are increasingly employed to establish the correct loading on the luminal surface of an artery, so that accurate stresses may be calculated within the vessel wall.

In the simplest implementation of CFD results into a solid mechanics computation, the data of the pressure field and wall tractions from a rigid-walled CFD simulation is mapped to the inner wall of the solid model geometry. The spatial discretizations of the fluid and solid domains, Ω_f and Ω_s, may be identical at the fluid-solid interface, or they may be different. In the case where the same discretization is used for both domains at the shared interface, a node-by-node passage of fluid variables to the solid models occurs. If the discretizations are different, an interpolation is made between the meshes, while some rule is put into place to ensure consistent integration of loads over the domains. From the natural geometry of the problem, it is obvious that Ω_f and Ω_s must lie within some tolerable distance ε of each other, such that their real-world contact is modeled. As just described, this is the traditional "one-way" or "weak" coupling scheme, in which fluid variables are passed only once to Ω_s, and then the FEM solver is run to calculate stresses and strains on Ω_s. Such a method works well for problems where the solid displacements are very small, and the deformed solid domain does not indicate an appreciable change of the boundary of the fluid domain, and therefore the CFD solutions. This method assumes a fluid-structure equilibrium is directly achieved, and there is no iteration between fluid and solid solutions to establish a rigorous, multi-domain equilibrium. The benefit of using such "weak" coupling is that fully separate solvers may be used for solid FEM solutions and CFD solutions, as long as an effective passage of variables occurs. Memory requirements for this approach are also little more than those of the separate solid and fluid solvers. The "one-way" coupling approach is often used in industrial applications, where solids are made of very stiff metals or composites and do not deform much under fluid load. Because we know that the typical blood vessel displays a nonlinear mechanical response and undergoes large deformations, "one-way" schemes are not appropriate, although they were used in the past due to computational constraints.

There are two alternative methods by which fluid and solid domains may be coupled in multiphysics finite element simulations, the direct method and the partitioned method. Both approaches are capable of strong coupling between Ω_f and Ω_s, such that a rigorous multi-domain equilibrium can be achieved in static or dynamic simulations. In the "direct" method of solving coupled fluid-structure problems, a single system of equations representing the fully coupled problem is constructed using a finite element discretization procedure. The entire system, which is necessarily characterized by a non-symmetric coefficient matrix due to the fluid equations,

is then solved using standard methods applicable to non-symmetric systems. Most problems in vascular mechanics involve geometrical discretizations that result in a large number of fluid and solid elements, and thus the number of equations to be solved simultaneously using the direct method can become quite large. Due to prohibitive computational memory requirements, the direct method for solving a strongly coupled fluid-structure problem is often not preferred, and a partitioned scheme is employed.

The partition method for solving fluid-structure interaction problems is an extension of the "one way" coupling method, and the *basic* approach is easily understood. The problem is characterized by three domains, Ω_f, Ω_s, and Ω_{fsi}, where Ω_{fsi} is the interface between the fluid and solid domains; in the typical three-dimensional vascular simulations, Ω_{fsi} is the three-dimensional surface where blood contacts the artery wall. The physics of the solid domain are the standard equations of motion in a Lagrangian frame.

$$\rho\frac{\partial^2 \boldsymbol{u}}{\partial t^2} = \nabla \cdot \tau + \boldsymbol{f}_B \qquad (28)$$

where ρ, $\boldsymbol{u}$, τ, and $\boldsymbol{f}_B$ are the local material density, displacement vector, Cauchy stress tensor, and body force vector. In many vascular mechanics fluid-structure interaction models, blood is considered to be an incompressible, isothermal, Newtonian fluid. In this case the equations of motion, the Navier-Stokes equations, are written as

$$\rho\frac{\partial \boldsymbol{v}}{\partial t} + \rho\boldsymbol{v} \cdot \nabla\boldsymbol{v} - \nabla \cdot \tau = \boldsymbol{f}_B$$
$$\nabla \cdot \boldsymbol{v} = 0 \qquad (29,30)$$

where $\boldsymbol{v}$ is the local fluid velocity vector and τ is the fluid stress tensor. As written, these equations are suitable for describing flow in an Eulerian frame. In FSI simulations, where the fluid domain is capable of deformation, and the computational mesh is not static, the arbitrary Lagrangian-Eulerian (ALE) frame is used to analyze flow. The ALE frame is intermediate between the "material-following" Lagrangian frame and the "spatial reference" Eulerian frame, and is characterized by an ALE frame velocity $\boldsymbol{v}'$ [71]. In an ALE frame, the Navier-Stokes equations are written as

$$\rho\frac{\partial \boldsymbol{v}}{\partial t} + \rho[(\boldsymbol{v} - \boldsymbol{v}') \cdot \nabla]\boldsymbol{v} - \nabla \cdot \tau = \boldsymbol{f}_B$$
$$\nabla \cdot \boldsymbol{v} = 0 \qquad (31,32)$$

Of course, we cannot hope to solve these equations without the application of suitable constitutive relations for the solid (we've assumed the fluid to be Newtonian), as well as physically meaningful boundary conditions. In an FSI simulation there are several different boundaries over which different conditions must be satisfied. On the purely solid boundaries, where there is no contact with the fluid domain, we have

$$u = u_{\Gamma_u} \text{ on } \Gamma_u \tag{33,34}$$

$$\tau \cdot n = f_{\Gamma_f} \text{ on } \Gamma_f$$

where Γ_u and Γ_f are the subsets of the purely-solid boundary where displacement and traction conditions are specified, respectively. Statements of the boundary conditions at the purely-fluid boundaries, where there is no contact with the solid domain, are more complex in the ALE frame. In the typical vascular mechanics FSI simulation, these boundaries comprise zones where velocities are specified, pressures are specified, or a more complicated (but more realistic) impedance function is specified. These zones do not overlap, and thus do not over-specify the problem. At the fluid-structure interface, Γ_{fsi}, the following boundary conditions must be satisfied

$$u_s = u'$$

$$\dot{u}_s = v \tag{35a, b, c, d}$$

$$\ddot{u}_s = \dot{v}$$

$$\tau_s \cdot n = \tau_f \cdot n$$

where u_s and u' are the solid and ALE displacement vectors, v is the fluid velocity, τ are stress tensors, subscript s denotes "solid", subscript f denotes "fluid", overscript dots denote time derivatives, and n are outward normal unit vectors. It should be noted that at Γ_{fsi}, the fluid velocity and the ALE frame velocity are equivalent. These conditions ensure that the fluid and solid domains remain in contact (appropriate for blood vessels), that a no-slip condition is enforced, and that Newton's third law is obeyed.

The *basic* solution strategy using the partitioned method is to first solve the fluid problem subject to the fluid-only boundary conditions, and the *initial* displacement, velocity and traction conditions on Γ_{fsi}. When the velocity and pressure fields are known, traction vectors are calculated at Γ_{fsi}, and are used as force boundary conditions on the solid domain. The force boundary conditions from the fluid tractions, and the solid-only boundary conditions are used to solve the solid system for the solid displacement and velocity fields. The displacements and velocities of the solid domain at Γ_{fsi} are used to deform the fluid mesh at Γ_{fsi}, and one of many schemes is used to adjust the interior nodal positions in the fluid mesh to maintain mesh quality. When the fluid mesh has been updated in terms of nodal positions and displacement and velocity boundary conditions, the fluid system is solved again. This entire procedure is iterated until convergence is reached in the solution vectors for the fluid and solid domains. This is done for every time step of the simulation.

As in the "one way" weak coupling method, the discretizations of the solid and fluid domains do not need to be identical at Γ_{fsi}. This is advantageous to the FEM user, as a much finer computational grid is often warranted in parts of the fluid domain, and would lead to excessive computation time and memory requirements in solving the solid system. There are many variations on this basic solution scheme, and several research and commercial finite element codes are capable of solving FSI

problems. The interested reader is pointed to [72, 73] for a more complete treatment of the theory and practical solution of these complicated and useful initial boundary value problems.

5.1   Stenotic Geometry, Healthy Material

One of the simplest vascular mechanics problems for which FSI simulation is truly needed is the simulation of flow through an idealized, single-layer, non-branching stenotic artery, such as the one shown in Fig. 4.

Because of this problem's material and geometrical simplicity, and its good approximation to a condition of biological relevance, several groups have studied this system experimentally and numerically. In the interest of brevity, only a few studies by Tang, Yang, Ku, et al, who have made extensive numerical analysis of this system, will be presented. For a more complete background of this problem, the reader is referred to the references in [74–77].

In [75] Tang et al studied a thin walled stenotic model, using a commercial finite element code to achieve a strongly coupled steady-flow FSI solution. The authors sought to identify the effects of stenosis severity and asymmetry on wall shear stress and the fluid pressure field, which was known to be complicated in stenotic geometries. Of particular interest to the authors were the critical flow conditions that might lead to vessel collapse due to severe pressure drop across the stenotic throat. The computational wall model was based on dimensions (78% stenosis by diameter) and material response of a silicone tube used in steady-flow experiments. The authors used a radial expression of the tube law, and Laplace's law to derive stress-strain relationships for the stenotic throat and segments proximal and distal to the throat, based on experimental observation. The stress-strain data were fit with a two-term Ogden model using a least squares approach; material homogeneity and incompressibility was assumed. The solid domain was discretized with eight-node hexahedra, and the fluid domain with six-node prismatic elements. The solid field equations assumed large displacements and the fluid domain referenced an ALE frame. Although the numerical model was based on a silicone experimental model, dimensions and flow boundary conditions were appropriate for flow in a carotid artery.

The authors analyzed the flow and wall displacement for stenoses between 20% and 90% that were 0% or 100% eccentric, using an inlet pressure of 100 mmHg and full-segment pressure drops of 10–100 mmHg. The data presented in the paper
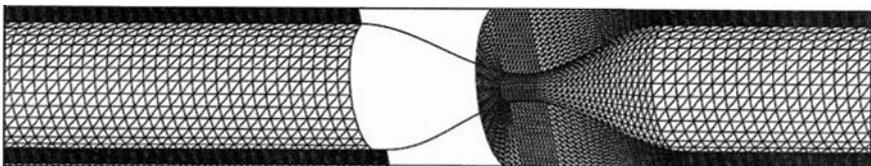
Fig. 4 FEM mesh of stenotic artery as used in Tang et al. [74]

were for 50% and 78% stenoses, using outlet pressures of 20 and 0 mmHg, which is in the physiological range of carotid stump pressures measured intraoperatively and reported by Hafner [78]. The studies demonstrated good agreement between numerical and experimental measures of volumetric flow rate versus total pressure drop, and showed the strong influence of stenosis severity and eccentricity on flow conditions. Under an equal outlet pressure condition, the magnitude of the (negative) minimum pressure at the throat, and the maximum wall shear stress were 36% and over 100% larger in the case of greater stenosis, while maximum flow velocities were similar. At constant flow rate, the maximum flow velocity in the lesser stenosis was about one sixth that of the more stenotic model. The maximum wall shear stress of the lesser stenosis dropped to less than a tenth of that of the more stenotic model, and the minimum pressure was no longer negativel; it was only about 2.5 mmHg below the outlet pressure. Loss of symmetry led to a lower minimum pressure at the stenotic throat and could represent an increased risk of arterial collapse. The maximum wall shear stress in the 100% eccentric model was 50% higher than that of the symmetric model, and can be easily understood considering the strong flow jet along the wall in that case. All models, symmetric or not, showed that the pressure and shear fields were complicated and three-dimensional. Similar studies were made in [74] for thick-walled models. The results were similar, but the studies focused more on quantifying the wall stresses due to the complex pressure field throughout the geometry.

Although both [74, 75] sought to characterize the critical flow conditions that could lead to vessel collapse at or just distal to the stenotic throat, neither study was well suited to predict this portion of the mechanical response. In [74, 75], the tube law was voiced in a specific radial form and maintenance of a circular lumen was implicitly assumed. This is contrary to experimental observations, where a pronounced loss of lumen symmetry accompanies vessel buckling. In [49], Tang et al performed numerical and experimental studies on a stenotic model made of a poly-vinyl alcohol (PVA) hydrogel. The PVA hydrogel was shown by to have a mechanical response similar to that of bovine carotid arteries [79]. In [49], the authors used an experimental tube law which does not directly specify the radius, nor make assumptions of maintained symmetry. Thus, the incrementally linear stress-strain relation derived from experimental pressure-area data was capable of better representing the response of the vessel under compressive stresses and in buckling or collapse conditions. Among the advantages of using the PVA hydrogel model was the ability to apply a physiological axial pre-stretch of 36.5%, where the silicone model of [75] was limited to a stretch of 2.4%. The authors used a generalized finite difference scheme to solve the fluid equations, a finite element method to solve the wall mechanics, and an incremental boundary iteration method to handle the fluid-structure interaction. Results were qualitatively similar to those in [74, 75], but the response under buckling and collapse conditions was much more realistic and compressive stresses were calculated more accurately. Again, comparison between 80% and a 50% stenosis models at the same flow rate demonstrated immense differences in shear stress magnitudes, maximum flow velocities, pressure minima and total segment pressure drops. Additionally, there were no compressive stresses

for the less severe stenosis, and the maximum compressive stress in the more severe stenosis was about 60% of the maximal tensile wall stress. In [77],Tang et al performed a series of similar numerical and experimental simulations on asymmetric, stenotic PVA hydrogel models. In this work, the authors performed mechanical testing on the isotropic, incompressible material in both tension and compression. The experimental data was used to fit a four-term Mooney-Rivlin material model, which represented the material response quite well even down to stretch ratios of 0.7. The use of a fully nonlinear material formulation, based upon direct experimental compression data allowed the authors to accurately study the deformation of the stenotic tube when pressures became negative at the stenotic throat. The many figures and data tables of [77] present a comprehensive stress and flow analysis of the stenotic model, and the interested reader is referred to the original work for a complete description.

6 Carotid Bifurcation

As explained in chapter 5, atherosclerosis is a focal disease that preferentially affects regions of the vasculature where disturbed flow or pronounced curvature are present. A detailed account of atherogenesis, from biological and mechanical perspectives can be found in chapter 5 and references later in this chapter. Because of its focal nature, and the ease (in some vessels) with which advanced lesions can be detected at autopsy, we have for a long time known about the common sites of atherosclerotic disease. Among the most common sites is the carotid bifurcation. The left and right common carotid arteries normally arise from the aortic arch and the brachiocephalic trunk, respectively, and continue without branching until approximately the level of the fourth cervical vertebra. At this level, each common carotid bifurcates into an internal carotid artery that supplies blood to the brain, and an external carotid artery that supplies more superficial anatomy. The representative dimensions of the carotid bifurcation are shown in Fig. 5. Note the widening of the internal carotid just distal to the bifurcation. This region, the carotid sinus, contains baroreceptors that detect and thus help regulate the systemic blood pressure. Because of the focal widening, and resulting flow patterns, the carotid sinus is a common site of atherosclerosis.

The carotid bifurcation is among the vascular segments most studied by clinicians and scientists investigating atherosclerosis, for at least four reasons. First, the bifurcation is a very common site for atherosclerosis and ischemic stroke is often caused by carotid disease. Second, at a depth of about 3 cm below the skin and remaining relatively still throughout the cardiac cycle, the bifurcation is better suited to medical imaging studies than other sites (i.e., the coronary arteries). Third, a definitive treatment for advanced carotid disease is carotid endarterectomy, a procedure that resects the diseased portion of the vessel, thus providing specimens for histological analysis. Fourth, the carotid's relatively little motion through the cardiac cycle makes it amenable to numerical modeling, as displacement boundary conditions are easily established and enforced. Because a great deal of vascular mechanics

modeling focuses on healthy or diseased portions of the carotid bifurcation, or on the entire structure, many of the remaining segments of this chapter will present studies on this region of the vasculature. The modeling techniques described, from imaging to segmentation, solid modeling, and analysis are not exclusive to the carotid bifurcation, and may be employed for other vascular investigations.

6.1 Healthy Carotid Bifurcation, Measurement-Based

Early studies of the carotid bifurcation were dedicated to flow analysis, and many features of these works were presented in the last chapter. Patterns of primary and secondary flow, and characterizations of wall shear stress were the focus of such work, as they were suspected to relate to the initiation of atherosclerosis. In order to more accurately predict flow patterns, and to shed light on the mechanics of the vessel wall, some investigators started to employ compliant artery walls in their bifurcation models. In [80], Perktold and Rappitsch coupled their 3-D flow model of an idealized carotid bifurcation to a geometrically nonlinear, incrementally linearly elastic, isotropic, nearly-incompressible shell model of the bifurcation wall. The geometry of the model was that of Ku et al. [81], and was based upon biplane angiography data from 57 patients aged 34–77. The 3-D Navier Stokes for incompressible, non-Newtonian flow were solved using a stabilized Galerkin finite element scheme, and the wall was loaded by the fluid pressure field through an iterative procedure at every time step of the cardiac cycle. The fluid domain was discretized with eight-node hexahedra tri-linear in velocity and piecewise constant in pressure. The shell model comprised four-node, reduced integration quadrilateral elements, with hourglass control. The shell thickness varied throughout the model to account for variable wall thickness in the real artery, and viscous stresses were not accounted for in wall loading. Although the wall model was rather simplified and the stress magnitudes could not be validated, the simulations revealed some important characteristics of carotid bifurcation mechanics. Tangential displacement of the shells was found to be small compared to the normal displacement, as expected, and maximal normal displacement was found in a small region centered on the flow divider. The stresses were calculated at the shell mid-surface, and were most significant at the apex of the bifurcation. The stress concentration factor, defined as local stress divided by nominal stress at the proximal common carotid, was 6.3 at the apex, and the stress gradients were large in the surrounding region. At the point of greatest normal displacement, the stress was surprisingly low and this was attributed to a stretchless membrane deformation.

In [82], Salzar et al studied the wall stresses in the carotid bifurcation to investigate their hypothesis that development of atherosclerosis is related to elevated intramural stresses. Other work had previously shown that low and oscillating wall shear stress was positively correlated to the development of atherosclerosis, and that high-shear, laminar flow was possibly atheroprotective.[3] The apex of the carotid

---

[3] See chapter 5.

bifurcation is generally a high-shear, laminar flow environment, and thus further investigation was needed to understand why this region was a fairly common site of atherosclerosis. Salzar et al performed a comprehensive analysis of the geometrical features of the carotid bifurcation by studying six cadaveric specimens, 76 angiograms, and ultrasound and MRI data. With a firm grasp of the normal variation of bifurcation geometry, the authors used photo-magnified visual data and measured silicone casts from two carotid bifurcations to build their finite element models. The 3-D geometries were divided by a noted approximate symmetry plane defined roughly by the centerlines of the common, internal, and external carotid arteries. The "half wall" geometries were discretized into surfaces of higher order shell elements, and the shell thickness was allowed to vary throughout the models to match the specimens. A normal pulse-pressure load of 40 mmHg was applied to the inner surface of the shell models, with the assumption that the material response was incrementally linear over this range and the stress patterns would be similar to those over the normal 80–120 mmHg physiological range. The wall was assumed to be incompressible and a parameter study was done over the range of incremental moduli of $14 \times 10^6 – 62 \times 10^6$ dyn/cm^2 published by Fung [83]. The authors calculated the mid-shell surface stresses over the geometry, and found an extreme stress concentration at the bifurcation apex. In addition to the high first principal (circumferential) stress magnitude at the apex, the spatial gradient of the stress was also noted to be very high. The stress concentration factor, defined as local first principal stress divided by nominal first principal stress at the proximal common carotid, was 9.2 and 14.2 at the apex for the two models. In addition to the stress concentration at the apex of each model, the outer wall of the carotid sinus was shown to be under higher than nominal stress, with stress concentration factors of 3.3 and 4.4 in the two models. The spatial gradients of these stress concentrations were not as steep as those at the apices, and a greater area of the wall was under elevated stress at the sinus. The authors noted that typical lesions of the bulb are large and well developed while those at the apex are more focal in nature, perhaps relating to the stress peaks and their gradients. Salzar et al. also noted that the remainders of each model, besides the apex and sinus, were near the nominal stress level, and atherosclerosis develops outside of the apex and sinus regions to a lesser extent. Although the authors stated that the stress patterns did not change much on modifying the overall wall thickness, no sensitivity analysis was made on the wall mesh, and thus only very qualitative results were obtained in this study.

The studies by Perktold et al [80] and Salzar et al [82] were important developments in investigations of carotid bifurcation mechanics, and were the basis for more advanced work. Because of the shell model formulation of the bifurcation wall, and the assumptions about material response, however, neither study was able to reliably calculate wall stresses in these complex geometries of variable thickness. One year after the publication of [80, 82], Delfino published a Ph.D. dissertation [19] which was, until that point, the most comprehensive stress analysis of the human carotid bifurcation. In the dissertation, Delfino used seven cadaveric carotid bifurcations in the unloaded state to make experimental observations and define an "average" finite element model of the bifurcations. Pressure-radius and axial force-radius data was

used to define the parameters a = 44.24623 kPa and b = 5434.8 in the Demiray-type strain energy density function presented earlier in this chapter.

$$W = \frac{a}{b}\left(e^{\frac{b}{2}(I_1-3)} - 1\right) \tag{36}$$

Geometrical data on the specimens, and from other studies provided the basis (see Fig. 5) for the 3-D bifurcation model without residual strains. The 3-D geometry of the model is shown in Fig. 6.

   The model was discretized with eight-node hexahedra using a large displacement, mixed finite element formulation. The material was treated as isothermal, isotropic, homogeneous, hyperelastic, and incompressible. The thickness of the wall was meshed with five elements throughout the model. Using a commercial finite element code, an axial stretch of 10% was imposed at the cut-surfaces of the internal and external carotid artery branches to match the *in vivo* condition. The cut-surface

Arc length	Distance [mm]
AB	6
BC	5
CD	5
DE	2.5
EF	2.5
FG	2.5
GH	6
BI	6.5
IJ	15

position	thickness [mm]	radius r; [mm]
A	0.9	3.1
B	0.6	3.1
C	0.6	3.3
D	0.55	3.3
E	0.52	3.15
F	0.49	2.7
G	0.43	2.2
H	0.4	2.2
I	0.6	1.83
J	0.4	1.83
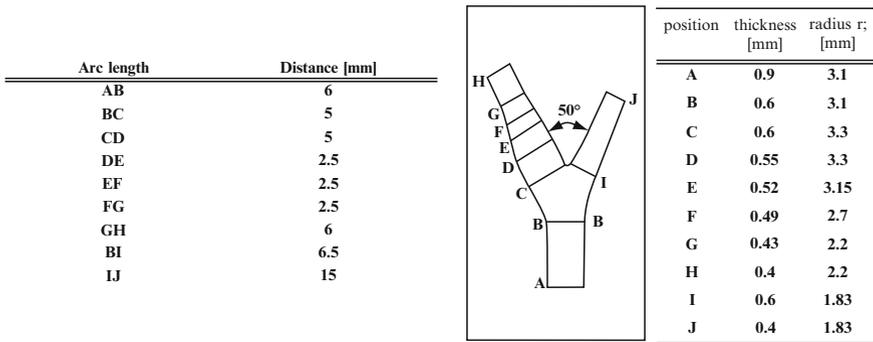
Fig. 5 Representative geometry of the human carotid bifurcation, as determined in [19]
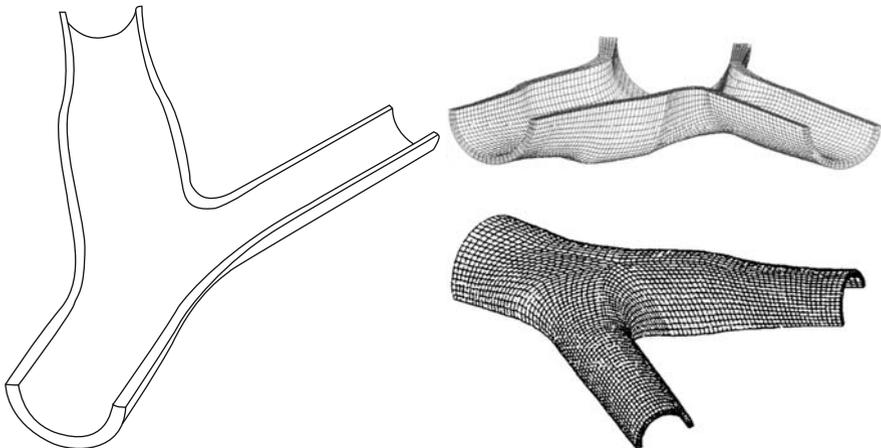
Fig. 6 3-D geometry of human carotid bifurcation (without residual strains) designed by Delfino [19]

of common carotid was held fixed in the local axial direction. With local cylindrical reference frames defined at the cut-surface of each branch, all branch ends were constrained in the axial and circumferential directions after the initial axial stretch was applied, and only radial displacement was allowed. At this point, a 120 mmHg pressure load was applied to the interior face of the full bifurcation model to simulate peak systolic pressure.

Similar to the findings of [80, 82], the highest first principal stress, 655 kPa, was located on the inner wall surface in the region of the bifurcation's apex, approximately 2 mm from the plane of symmetry. Unlike the earlier findings, however, Delfino's model utilized a fully three-dimensional element and could more accurately calculate the stress throughout the thickness of the wall. Delfino called the ratio of the local wall stress to that at the outer surface of the wall in the same location the "uniformity factor". At the location of maximum stress, the uniformity factor was the highest in the entire model at 8.8. A secondary stress concentration, peaking at 340 kPa, was noted at the junction of the common and external carotid arteries, and the uniformity was near 3.0. Throughout the model, stresses were highest on the inner surface, and lowest at the outer wall surface with values ranging from 63 to 80 kPa. The first principal stress at the proximal common carotid artery was 148 kPa, and thus the stress "concentration factor" of Perktold and Salzar would have been 4.42 at the apex stress peak. The stress at the carotid sinus was not discussed explicitly, and from the original figures does not look locally elevated, as reported in [80, 82]. The uniformity factor at the carotid sinus was 2.7. From the data and figures provided, the stress at the inner wall of the carotid sinus appears to be within the range of 175–220 kPa, and thus is not the second largest stress concentration as was suggested by the studies of Perktold and Salzar.

Residual strains, and the assumed strain-free reference state can have a large impact on the stresses calculated in a finite element model, and are shown in Fig. 2 to drastically change the maximum stress and intramural stress gradients in the case of the rabbit common carotid arterial segment. Because of the complex geometry of the carotid bifurcation, a thorough understanding of the strain-free state and the residual stresses in the unloaded state are difficult to obtain, and had for a long time been ignored in studies. To characterize the residual stresses, Delfino [19, 84] made a series of cuts in the unloaded, undiseased bifurcation and observed the subsequent change in geometry to discern the strain-free state of both human and porcine carotid bifurcations. The first cut was on a plane that roughly halved each branch and was considered to be an approximate symmetry plane of the full bifurcation. After this cut was made, the cut edges of each branch remained co-planer with each other, and the apex of the bifurcation rose into a "bump". No further cuts caused significant geometrical changes, and the shape after the first cut was taken to be that of the strain-free state. The observation of co-planarity of the cut edges was used, along with the assumption of material incompressibility, to define relations between the opening angles and radii of the three branches in the strain-free state. With these relations, the opening angle and strain-free radii of the internal and external carotid arteries could be determined from measurements of the thickness and radius of all three branches in the unloaded state, and an opening angle of the cut

common carotid artery. The opening angle and radii predictions from this method were shown to match well with experimental observations. With this method, and experimental data, Delfino constructed a strain-free finite element representation of the bifurcation. The loading that would deform the strain-free state into the un-loaded, but residually stressed state was determined and applied to the strain-free model. After this initial deformation was accomplished, 10% stretches in the local axial directions were applied to the internal and external carotid arteries, and then the model was pressurized to 120 mmHg.

The inclusion of residual stresses into the model had a significant impact on the uniformity factor throughout the model, and affected the maximum principal stresses predicted. In the model with residual stresses, the peak stress was again near the apex, but the stresses in that region were much lower (from 132 to 221 kPa), and the area over which stresses were raised was much more localized than in the model without residual stresses. Whereas the model without residual stresses had a uniformity factor of 8.8 at the apex stress peak, the residually stressed model had a uniformity factor of 1.16 there. The highest uniformity factor occurred at the lateral wall of the carotid sinus, and was 4.1. The nominal uniformity factor at the proximal common carotid artery was 1.1 when residual stresses were taken into account, compared to 3 when they were not, and the outer wall stresses were nearly a factor of two greater in the residually stressed case. Thus, the inner wall stresses were generally reduced by a factor of nearly 1.5 when residual stresses were included. Although other studies had hypothesized that wall stress magnitude was associated in some way with atherogenesis, Delfino investigated whether or not the local uniformity of stresses throughout the wall thickness was involved with development of the disease. To do this, Delfino compared the uniformity factor data from the residually stressed model to intimal thickness data from Ku et al [81]. Intimal thickening is associated with early stages of developing atherosclerosis. When all 15 regions studied in [81] were used in the comparison, uniformity factor and intimal thickness were shown to correlate well, with $r = 0.84$, $p < 0.05$. When sub-groups of regions were studies separately the correlation was even higher with $r = 0.99$, $p < 0.001$, especially in the carotid sinus, where atherosclerosis commonly develops. Thus, Defino's study suggested that the uniformity of stress magnitude through the wall may be a localizing factor in atherogenesis. A great deal of work to characterize the human carotid bifurcation is contained in [19], and the reader is referred there for further information. Of note is the study on inhomogeneity of material properties throughout the bifurcation. The essential effect of considering the non-uniform collagen content of the wall is that the stress at the outer wall of the apex is increased by nearly a factor of 2 and remains largely unchanged elsewhere.

The model built by Delfino [19], based in part on data from Bharadvaj et al [85], is recognized in the literature as being a realistic idealization of the human carotid bifurcation. Several groups have used the same geometry as the basis for their own finite element investigations in carotid bifurcation mechanics. Although the study focused on flow characterization under resting and exercise conditions, Younis et al [86] used the Delfino model without residual strains to build a fluid domain, and performed FSI simulations with the same material formulation, axial pre-stretches, and

solid boundary conditions used in [19]. Hariton et al [87] used the Delfino model without residual stresses to investigate the effects of a materially inhomogeneous carotid bifurcation, although the investigation took a very different approach than that in [19]. Hariton et al, used the isotropic version of the strain energy density function given in Eqs. (21–23) to test their hypothesis that collagen fiber orientation is actively remodeled *in vivo* such that the mean fiber direction is aligned with the tensile maximum principal stress. It should be noted that the isotropic version of the two-fiber family model in Eqs. (21–23) is only slightly modified from the isotropic strain energy density function employed by Delfino, containing an additional neo-Hookean term. The motivation for the hypothesis of fiber alignment to maximum principal stress direction was the experimental observations of mostly isotropic response for embryonic tendons and arteries, yet pronounced collagen fiber organization after directional load conditioning, and thus an anisotropic response.

The basic method of the study was to perform a finite element stress analysis of the bifurcation with an isotropic material formulation, and axial stretches of the three branches that were modified from those in [19]. When the two largest principal stresses, in directions $\hat{e}_1$ and $\hat{e}_2$ respectively, were identified throughout the model, the local fiber directions were defined as

$$
\begin{aligned}
a_{01} &= \cos \gamma \hat{e}_1 + \sin \gamma \hat{e}_2 \\
a_{02} &= \cos \gamma \hat{e}_1 - \sin \gamma \hat{e}_2 \\
\tan \gamma &= \frac{\sigma_2}{\sigma_1}
\end{aligned}
\tag{37}
$$

and the model was updated to include the material formulation of Eq. (23) using these fiber directions. The static finite element problem was then solved again, this time with the updated material formulation accounting for fiber alignment. This procedure was iterated until a suitable convergence was reached in principal stresses at the apex and mid-sinus point. Convergence within 1% was reached after only eight iterations, and the predicted fiber orientations agreed well with histological observations from cerebral arterial bifurcations. The results reached at convergence were shown to be independent of starting fiber orientation distribution, although no rigorous convergence analysis was made. Fiber alignment along the apical ridge, or saddle, occurred during the iterative process, leading to the same "tendon-like" collagen structure noted by other experimental work. Validation of the remodeling fiber model was performed by comparing the predicted fiber orientations of the roughly cylindrical proximal CCA and distal ICA and ECA to the predicted orientations through the thickness of an ideal cylinder vessel. The predictions from the full bifurcation model compared very well with those from the ideal straight segment, indicating the stability and accuracy of the model. The high stress predicted at the apex was about an order of magnitude larger than that at the inner wall of the cylindrical portions of the bifurcation. This result compared favorable to an analytical estimate, and also to data obtained from collagen polarizing microscopy analysis, where a known correlation between collagen birefringence and material properties was exploited. Hariton et al also calculated the uniformity factor throughout the bifurcation, and the results were in the range of those found by Delfino. Of note is

the fact that the uniformity factor at the medial aspect of the junction of ICA and CCA was nearly 1, whereas the uniformity factor at the lateral wall of the sinus was twice as great. This finding supports the hypothesis that intimal thickening known to occur at the lateral sinus serves to homogenize the stresses through the arterial wall, while intimal thickening is less often found at the medial aspect of the sinus.

7 Patient-Specific Studies

While much has been learned from creative and detailed studies on idealized vascular structures, it is of great interest to draw more quantitative and specific conclusions about the relationship between mechanical environment and disease initiation and progression. With regard to atherosclerosis at the carotid bifurcation, the mechanical factors of interest are the flow-induced wall shear stress and wall stresses and strains, while the macroscopic biological indicators of initiation and progression are intimal thickening and plaque growth and rupture, respectively. There are additionally a host of cellular and biochemical indicators of disease initiation and progression, and their relation to mechanics is of fundamental importance.

Among the many conclusions drawn from studies of idealized vascular structures is that the flow velocity and pressure fields, and mechanical stresses and strains of the arterial wall can be quite sensitive to even small changes in geometry and material response. Thus, to make meaningful quantitative analyses of the relationships between mechanics and biology, the obvious system to study is the real blood vessel, in healthy and pathological conditions, as it exists *in vivo*. Complex geometries, difficult or impossible to discern material properties, and complicated *in vivo* boundary conditions make the patient-specific blood vessel a difficult system to study. Much progress has been made in recent years to address these challenges. The remainder of this chapter will discuss the complications of modeling an *in vivo*, patient-specific vessel, and publications that demonstrate the tremendous progress in computational vascular mechanics will be presented. It is instructive to first briefly review the imaging tools most commonly employed in patient-specific vascular studies.

8 Imaging-Derived Geometry and Flow Boundary Conditions

Patient-specific modeling requires a delineation of the geometric morphology of the vascular lumen, of each of the components in the vessel wall, and of the outer wall boundary. In addition, it is important to know the time-varying velocity profile across each of the vessels that provide flow into the volume of interest. Finally, accurate assumptions must be made about the pressure conditions in the outflow vessels. Much of this information can be obtained with little or no invasiveness using modern medical imaging methods. CFD and solid mechanics models require a three-dimensional rendering of the structures of interest. This is conveniently obtained using x-ray based or magnetic resonance (MR) techniques.

8.1   *Computed Tomography*

Computed Tomography Angiography (CTA) is a robust method for attaining large volume coverage with uniform signal intensity in the flow lumen in relatively short acquisitions [88, 89]. Data sets are acquired following the intravenous injection of a contrast agent which opacifies intralumenal blood. Once arrival of the contrast agent in the vascular segment of interest is detected, x-ray transmission data is acquired from a series of thin slices covering the vasculature of interest. The data from these slices can be reconstructed to provide a stack of contiguous images constituting a three-dimensional volume of data. Typical resolution in these studies is of the order of 0.4 mm along each axis and the total acquisition can be performed in under 10 s. Following contrast injection, the vascular lumen is depicted with strong contrast to adjacent soft tissue, which facilitates segmentation of the flow channel. The ability to uniquely identify different materials in a CTA study depends on the relative strength of absorption of x-rays of each component. In this regard, calcific deposits have high absorption and the presence and distribution of calcified plaques can be readily determined. It is more difficult to discriminate between other components of an atheromatous plaque, but progress has been made in using this modality to differentiate the necrotic lipid core from fibrous components of the plaque. As has been noted, materials that are strong absorbers of x-rays also have high signal intensity and this can be a drawback for CTA as it can be difficult to separate bone from vessel if those two structures are close together. Similarly, metal in the body, such as surgical clips or dental fillings, can generate pronounced artifacts which obscure blood vessels. Finally, CTA carries a risk of deleterious effects from the contrast agents used which are poorly tolerated by patients with compromised renal function, and from the x-ray dose. For this reason, CTA is not the method of choice for research studies or for studies that require multiple follow-up examinations. For those applications, MR imaging is the preferred method. Figures 7a and 7b show axial and sagittal imaging data, respectively, for a carotid bifurcation with a large plaque burden.

8.2   *Magnetic Resonance Imaging*

MR imaging methods rely on the detection of magnetization arising from the nucleus of hydrogen atoms in water [90]. All MR angiographic techniques aim to create high contrast between spins that are moving and those that are stationary. MR imaging methods are capable of measuring both the magnitude of the transverse magnetization and the orientation of that magnetization in space (the phase). Methods have therefore been devised that are designed to create large differences either in the magnitude or in the phase of the magnetization between spins that are stationary and spins that are moving. MR sequences that rely on blood flow to transport fully magnetized blood into the imaging volume and thereby create a substantial difference between the magnetization of flowing and stationary spins are generally referred to as time-of-flight (TOF) methods and they display the magnitude of the
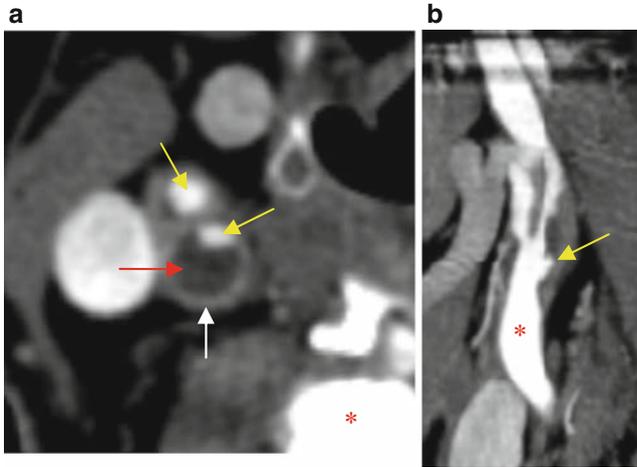
Fig. 7 (**a**) Axial CTA showing vessel lumens (*yellow arrows*), vessel wall (*white arrow*) and large plaque (*red arrow*). Note the high signal intensity of the vertebral bone (asterisk). (**b**) sagittal reformation of the CTA data showing flow lumen (asterisk) and ulceration of atheroma (*arrow*)

transverse magnetization. Sequences that rely on the presence of contrast agents injected into the blood stream to enhance vascular signal are referred to as contrast-enhanced MRA (CE-MRA), and also create images that display the magnitude of the transverse magnetization. Images that display the phase of the magnetization are referred to as phase contrast (PC) images. These methods rely on the motion of spins with respect to the imaging gradients for vessel-to-stationary tissue contrast.

8.3 Time-Of-Flight (TOF) Methods

The contrast that is obtained in an MRA study is closely related to the strength of the magnetization in flowing blood relative to that in stationary tissue [91]. MR angiograms are built up by repetitive sampling of the magnetization. The strength of the magnetization of spins decreases with each sampling until it reaches a steady state value that is determined by the measurement parameters; the flip angle, the repetition time, and the T1 relaxation time for that tissue. This process is referred to as saturation. Stationary material remains in the imaging volume throughout data acquisition and, therefore, the magnetization strength of stationary spins decreases to the steady state value. The magnetization of blood at a given location in the vasculature depends on how much sampling it has experienced between entering the imaging volume and reaching that location. Fast moving blood may retain substantial magnetization strength. Slowly moving spins may have undergone many sampling intervals and its magnetization may, like stationary spins, also drop to the steady state value. In magnitude images, spins that have received many RF pulses and are strongly saturated will appear dark, whereas spins that retain substantial magnetization strength will appear bright.

8.4   2-D TOF Methods

Sequential 2-D TOF is a strategy that acquires the data one slice at a time. By making the slice very thin, it is ensured that the slice will be replenished with blood that has not undergone any prior sampling and that is not in the sampling volume long enough to become saturated. Each single slice acquisition requires a time on the order of eight seconds. The in-plane spatial resolution is typically 0.5×0.5 mm with slices that are 2 mm or thicker. The sequence can be repeated multiple times, each time shifting the position of the slice to permit the acquisition of a large set of consecutive slices in a reasonable imaging time. High signal contrast is attained between blood vessels and the stationary surrounding tissue. This procedure provides a full three-dimensional data set. Sequential 2-D TOF techniques provide strong inflow enhancement when the slices are perpendicular to the vessels of interest. When vessels run in the same plane as the slice, or reenter the slice, the blood becomes saturated and contrast is progressively lost. For this reason, the method is most effective when the vessel of interest runs in a straight course. Although 2-D TOF methods provide robust, high signal intensity with strong contrast between intralumenal blood and surrounding tissue, the poor spatial resolution along the slice direction reduces the applicability of this method.

8.5   3-D TOF Methods

The use of 3-D techniques overcomes the slice resolution limitation and permits the acquisition of a full 3-D data set with isotropic voxels that have typical dimensions of close to 0.5mm along each axis [92]. High-resolution voxels are critical for the visualization of small branch vessels, which might otherwise be obscured by partial voluming where a single voxel contains components both from the flow channel and from soft tissue. The isotropic voxels also provide clear depiction of tortuous vessels with equal fidelity in each spatial dimension permitting data reformation in arbitrary obliquities. In acquiring data from a 3-D volume the excitation volume is chosen to be a thick slab (or multiple thick slabs) with each slab of the order of 40 mm thick. 3-D acquisitions require markedly longer acquisition times than do 2-D methods but provide advantages in increased SNR. In 3-D acquisition, blood flowing through the excitation volume undergoes substantially more sampling than is the case for 2-D imaging. To avoid excessive saturation effects, the flip angle must be reduced ($<30°$), and, although good contrast is retained, this adjustment results in increased signal from adjacent stationary tissue. There have been reports that this ability to visualize some aspects of the vessel wall can be used to investigate important features of the atherosclerotic process, such as thinning or rupture of the fibrous cap. 3-D TOF images have good spatial resolution but are subject to inconsistent intralumenal signal resulting from patient motion or flow-related artifacts.

8.6   Phase Contrast MRA/MRI

As described above, time-of-flight methods engender strong contrast between vascular blood and stationary material by rapidly sampling all magnetization within a volume of interest thereby strongly suppressing signal from stationary material. Only blood vessels that bring blood with full magnetization into the sampling volume retain substantial signal strength. A different class of MR methods, termed phase contrast MRI, uses an approach where, in the interval between sampling pulses, the displacement of magnetization through the magnetic field gradients is encoded in the orientation of the magnetization vector [93]. Using this encoding, the orientation of the magnetization, or phase, is proportional to the velocity of blood flow. The signal from stationary material can be eliminated by acquiring two measurements with opposite phase encodings and subtracting the two data sets. Because of this mechanism, signal from background material is nearly eliminated and phase contrast angiograms can be acquired with considerable coverage. Although phase contrast methods can be used to create MR angiograms, their particular power resides in their ability to measure the velocity of blood flow. A common application for phase contrast velocity measurements is to determine velocities in a thin slice oriented perpendicular to the vessel of interest. It is straightforward to measure the component of velocity perpendicular to that slice on a pixel-by-pixel basis at fixed intervals through the cardiac cycle. With this approach, the velocity waveform in the target vessel can be determined with a temporal resolution of around 30 ms. In recent years, a number of investigators have explored the ability to determine all three components of the velocity vector, at all points in a 3-D volume, at multiple points in the cardiac cycle. These data sets provide interesting insights both into qualitative and quantitative features of the velocity field. MR velocity methods are convenient tools for determining the flow boundary conditions needed in CFD simulations.

8.7   Contrast-Enhanced MRA (CE-MRA)

The injection of intravenous contrast agents, such as Gd-DTPA, result in a strong reduction in the time that sampled blood requires to reestablish full magnetization. This means that contrast-enhanced blood will rapidly recover magnetization and will have high signal strength, even for short values of the repetition time. In order to perform a CE-MRA study, it is important to time the MR data acquisition so that it coincides with the period during which there is peak arterial signal. After reaching a peak, the arterial signal strength drops and venous signal starts to increase. Appropriate timing of the initiation of data capture is therefore of key importance and can be achieved using a test bolus to measure the time interval between injection and peak magnetization enhancement in the region of interest. The full study is then performed using the knowledge of the time delay between injection and peak magnetization strength. Alternatively, an automated method can be used to determine when the injected material arrives in the volume of interest and signal enhancement exceeds a preset threshold, at which point the CE-MRA study is begun.

In most applications, it is important to be able to acquire a 3-D CE-MRA study in a short time. This includes the extracranial carotid arteries, where there is a short interval when the first pass of the bolus provides maximal intra-arterial signal and when the venous enhancement, which occurs shortly after the arterial phase because of the blood-brain barrier, has not yet occurred. Similarly, short acquisition times are desirable for the vessels of the abdomen, so that studies can be obtained within a breathhold. Typical CE-MRA studies can now be performed in acquisition times from 10 to 20 s. However, the spatial resolution in MRI increases with the number of times the magnetization is sampled, and the requirement that data be captured while the contrast agent is still in the arterial phase results in CE-MRA images having relatively low resolution. Typical resolution in a CE-MRA study is then $0.5 \times 0.5 \times 1.2$ mm. Despite this shortcoming CE-MRA provides high contrast images that are generally free of the artifacts that result from flow-related effects [94].

8.8 Black Blood MRI

The MR angiographic methods described above are intentionally designed to highlight flowing blood. Images obtained using such methods can be found in chapter 5. Soft tissue, including the vessel wall, is only poorly delineated using these sequences. The great majority of MR methods that have been used to investigate the geometric and compositional morphology of the vessel wall rely on standard MRI methods for imaging soft tissue, namely spin echo sequences. In spin-echo sequences, the image strength of each soft tissue component can be adjusted by manipulating the timing and type of radiofrequency pulse used. The approach that has had most widespread application is the use of pulses designed to eliminate signal from all tissue apart from that in the slice of interest. This is termed double inversion preparation. In analogy to time of flight methods, the signal strength of intraluminal blood in the slice of interest reflects the magnetization state that is transported into the slice by newly arriving blood [95]. Double inversion preparation can be designed such that magnetization of blood outside the slice of interest reaches a null condition, and these images therefore have a black lumen. In addition, fat saturation preparation is used to suppress signal from adipose tissue. Spin echo sequences can be created with the usual contrast weighting employed in routine clinical imaging, referred to as T1, T2 or proton density weighting. A number of investigators have demonstrated, in comparison to histology on excised specimens, that combinations of these multi-contrast images can be used to define the major components of the atherosclerotic plaque including the fibrous cap, the lipid pool, calcifications, and intra-plaque hematoma. Figures 8a and 8b show representative images from such studies. The image resolution in these image sets is of the order of $0.5 \times 0.5 \times 2$ mm. These data sets can be used to construct models of diseased arteries but with a similar caveat as to that for 2-D TOF methods, namely that there is low resolution along the slice axis.
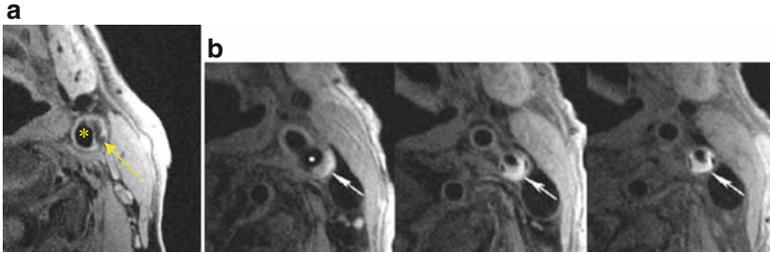
Fig. 8 (**a**) T2-weighted DIR fat saturated, Fast Spin Echo sequence shows a low intensity lipidic core (*arrow*), separated from the flow lumen (*asterisk*) by a thin fibrous cap. (**b**) T1-weighted DIR fat saturated, Fast Spin Echo sequence shows three contiguous slices through the extracranial carotid arteries. The internal carotid artery (*arrow*) is visualized showing the black lumen (*asterisk at the bifurcation – left image*) and surrounding atheroma with calcific inclusions (*black lines in the atheroma*). The middle and right images are from more distal levels

8.9 Ultrasound

MR and CT are relatively expensive modalities that are only available in fixed locations. Ultrasound (US) is portable and can be used on many patients who have contraindications to MR (such as pacemakers or claustrophobia) or CT (such as contrast agent allergy), and is therefore often the preferred modality for screening examinations. Ultrasound can be used in different modes with B-mode, color mode, and Doppler as the most common modes used in vascular examinations. B-mode imaging builds up a grey scale image of soft tissue interfaces by transmitting ultrasound pulses into the body and detecting the time of return of echoes reflected off those interfaces. Depending on the frequency of transducer used, in-plane spatial resolution in US images is of the order of 0.5 mm. Because US is a hand-held modality, it is impractical to build up a three dimensional data set from multiple images as their relative locations in space are unknown. In color mode, information that is collected on the direction of motion of flowing blood is color encoded and superimposed on the B-mode image. These spatial maps of the vascular structures can then be used to identify locations where velocity waveforms can be measured using Doppler US (DUS). With DUS, an insonation volume is placed in a desired location, for example, in the center of the vessel of interest. The full spectrum of flow velocities within the insonation volume can be determined with a high temporal resolution that is on the order of 10 ms. Using this approach the velocity waveform at a point can be accurately determined through the cardiac cycle. These measures can then be used for setting the physiologic boundary conditions in CFD simulations on a patient-specific basis.

8.10 Image Segmentation

Patient-specific computational models require a determination of the geometric boundaries of all constituent of the blood vessel of interest including the flow lumen, and all tissue components in the vessel wall. The ability to perform accurate and reliable segmentation of three-dimensional medical imaging data sets depends on the spatial resolution of the data, and the contrast between the different components – the higher the contrast the easier is this task. Manual contouring of different components can be effective using expert readers to determine the boundaries of different components. However, depending on the size of the data set, this can be a very tedious and labor-intensive task that can result in fatigue-related contouring errors. With sufficient contrast, simple thresholding can be applied to establish the contours of each component. This is typically applied on each slice of a 3-D volume, and lofting between one slice and the next can be accomplished using spline interpolation algorithms to form surfaces of all components through the 3-D volume. In cases where contrast between different components is not sufficiently high to unambiguously identify the location of the interface, more advanced image processing algorithms can be applied. A wide variety of methods have been employed including: the level set method that permits numerical investigations of surfaces without requiring that the surface has a parametric description; methods that interrogate geometric features of boundaries such as intensity gradients; or methods that minimize an energy function such as active snake contouring which use constraints on features such as smoothness and intensity patterns to determine the boundary contour.

9 Image-Based Modeling of Healthy Vessels

As discussed in the chapter 5, CFD of the patient-specific carotid bifurcation often makes a rigid-wall assumption. The geometric information needed for these models is limited to an accurate depiction of the luminal surface of the vessel, and various forms of angiography have been used with great success. While much has been learned from these studies, the assumption of rigid walls may not be suitable for flow analysis in carotid arteries, where radial distension of the healthy artery may be on the order of 10%. Additionally, this approach will yield no useful information of the solid mechanics of the vessel. To model the solid mechanics aspects of the artery, detailed knowledge of the luminal and outer adventitial surfaces of the vessel are required at minimum, and allow the vessel to be treated as a single layer of tissue. For a more realistic 2-layer model, delineation of the media-adventitia interface must be made as well.

In [96], Zhao et al used a combination of MRA and ultrasound to define their compliant-wall carotid bifurcation model, the subject was a healthy 40 year old male. A 2-D time-of-flight MRA study yielded 64 contiguous 1.5 mm thick slices, roughly centered on the bifurcation, from which a 3-D reconstruction of the vessel lumen was made. B-mode ultrasound imaging was used to establish representa-

tive thicknesses of the vessel wall at the proximal CCA, distal CCA, and the distal portions of the ICA and ECA. The boundary of the vessel lumen at each slice was segmented using a "snake" active contour algorithm. The centerlines of the vessel branches were constructed and fit in a least-squares sense with cubic splines, and then the 2-D contours were shifted in-plane so that the lumen centroids coincided with the spline location at every slice. This gave an axially smoothed representation of the bifurcation. Mapping of the 3-D Cartesian data into local cylindrical frames (r, z, φ) and subsequent smoothing of radius r over the local z-φ plane effected smoothing of the entire luminal surface. Interpolation across slices was used to construct a set of locally-axial B-splines and thus a surface description appropriate for mesh generation was achieved. A multiblock approach was taken in generating a structured grid of the bifurcation using hexahedral cells suitable for the study's finite volume CFD methods. The luminal surface used to make the fluid grid also served as the boundary on which a grid of shell elements was generated to represent the arterial wall. Each shell element's thickness was either taken to be one of the measured representative thicknesses, or an interpolated value between them. The incremental Young's modulus in the range of diastolic to systolic pressure was determined from time-resolved ultrasound data collected for the subject.

Pulsed Doppler ultrasound was used to establish the flow division between the ICA and ECA and the flow velocity waveforms at the ECA and ICA, which were the outlet boundary conditions on the flow domain. Applanation tonometry was employed to measure the pressure waveform at the CCA, which was the fluid inlet condition for the CFD simulation. The fluid domain used a moving grid approach to handle the motion of the inner wall boundary. Zhao et al used two separate commercial codes to perform the numerical simulations, a finite volume solver for the fluids, and a finite element solver for the solids. At every timestep of the transient simulation, iteration between the two codes enforced the FSI boundary conditions stated in Eq. (35). Only pressure was passed from the fluid domain to the solid domain, as viscous stresses were known to be much smaller.

In both [96] and [97] Zhao et al took a comprehensive approach to modeling the carotid bifurcation of a specific patient, collecting data on geometry, material response, and flow boundary conditions through various forms of medical imaging. The authors noted that the inclusion of wall compliance changed the extent, and the duration of slow moving or recirculating flow within the bifurcation. Additionally, the distributions and magnitudes of wall shear stress were shown to differ when wall compliance was considered, the changes being most pronounced around peak systole. The authors also noted the important result that secondary flow patterns are significantly modified when a realistic and non-symmetric geometry is modeled. This could, for some geometries and flows, lead to significant differences in wall shear stress distribution and must be considered if a detailed correlation between mechanics and endothelial biology is to be made. In [97], the authors performed the FSI analysis for five healthy subjects, and further noted the sensitivity of flow patterns and wall stress magnitudes and distributions on the geometrical and physiological features of the patient. One result common to each subject was the overlap of high wall tensile stress and low wall shear stress in regions that are known to

preferentially develop atherosclerosis, indicating that both fluid and solid mechanics may play a role in disease initiation.

In [98], Younis et al employed similar strategies to model the carotid bifurcations of three healthy subjects. An ECG-gated 2-D black-blood spin echo MR study was used to image the vessel wall at twenty slices centered on the bifurcation. In-plane resolution was 0.39 mm and slice thickness was 2 mm. The imaging data was processed to estimate inner and outer wall contours, defined by deformable splines, that were anisotropically smoothed through minimization of a surface energy in an external potential field. The inner and outer wall contours were used in a lofting procedure in a solid modeling code to generate parasolid models that could be discretized directly by a finite element preprocessor. The same techniques were used to create a fluid domain and a solid domain for FSI simulations. Flow profiles at the inlet and outlets of the model were generated using a Womersley profile assumption and scaling based on centerline velocities obtained from Doppler ultrasound studies on the subjects. The solid domain was meshed with 11-node tetrahedral elements suitable for large strain analysis of incompressible, hyperelastic materials. Vessel wall response was modeled using the Mooney Rivlin material formulation, and the material parameters presented in [19]. The fluid field was meshed with four-node tetrahedra linear in velocity and piecewise constant in pressure. A commercial finite element code was used to perform the fluid-only, solid-only, and FSI computations.

A comparison between the rigid-wall models and the compliant wall models revealed that wall compliance had a small effect on wall shear stress patterns (except at the apex, where differences up to 25% were noted), but an appreciable effect on the magnitude of oscillatory shear index (OSI). OSI is a measure of how much a particular region of the wall experiences flow in a direction against that of the temporal mean wall shear stress vector, and high OSI has been correlated with elevated monocyte adhesion and atherogenesis. The authors noted that wall distensibility generally increased OSI by a factor of two throughout their model. The solid-only models showed that cyclic strain, the difference between von Mises strain at systolic and diastolic pressures, was highest for all three subjects at the apex of the bifurcation. Cyclic strain is related to endothelial cell and smooth muscle cell proliferation, and to the migration of smooth muscle cells in the vessel wall. The upregulated proliferation of endothelial cells is thought to increase the permeability of the artery wall, and thus render it more susceptible to atherogenesis. Elevated maximum wall shear stress temporal gradient, and cyclic strain were co-located at the apex and the transition region between the CCA and ECA, two sites that commonly develop atherosclerosis. The authors note that this may suggest that atherosclerosis is promoted by several factors and that no one mechanical descriptor can fully account for atherosclerotic lesion distribution. The references in [98, 99], and in chapter 5 provide an excellent review of the relationship between mechanical environment and cellular and biochemical processes that are thought to promote atherogenesis.

There is much ongoing work to elucidate the complex biochemical and cellular mechanisms of atherogenesis, and their relation to local hemodynamics and solid mechanics. It is likely that modeling approaches that account for the direct influence of mechanics on biology will shed a brighter light on the specific conditions un-

der which atherogenesis is promoted. Such models would necessitate many further *in vitro* and *in vivo* studies to characterize the cellular response to mechanical stimuli. The acute conditions associated with atherosclerotic disease, such as stroke and myocardial infarction, are due to a thromboembolic event following plaque rupture or ulceration. Although there is significant biochemistry involved in weakening of a lesion, rupture and ulceration are inherently mechanical processes. Thus, an understanding of the mechanical environment of the atherosclerotic vessel is needed.

10   The Atherosclerotic Artery Wall

Atherosclerosis is a slowly progressing disease characterized by the accumulation of material within the artery wall. The disease is typically initiated in adolescence, and is seen with greater frequency with increasing age. Atherosclerosis preferentially affects larger arteries, and its presence has been correlated with local hemodynamic complexity. Specifically, it has been shown that regions of the vessel wall experiencing low and oscillatory wall shear stress are more likely to develop atherosclerotic lesions [81]. Presumably, this is due to shear-dependent alterations in the arrangement and permeability of the endothelial cells at the lumen surface [100–102]. Atherosclerosis is recognized pathologically to be an ongoing inflammatory response to local endothelial dysfunction, which may be caused by any combination of several factors. In addition to flow-induced shear stress, some of these factors are local infection, oxidative stress, chronic hypertension, and most notably, elevated low-density lipoprotein (LDL) levels [103]. At the dysfunctional endothelium, LDL is allowed to pass into the vessel wall, where it is oxidized by reactive oxygen species. The reactive oxygen species are present naturally, and in increased concentrations when the patient is exposed to one or more atherosclerosis risk factors. An inflammatory response to the oxidized LDL is mounted, and monocytes are recruited locally through the expression of various inflammatory mediators. Low mean or oscillatory wall shear stress tend to coincide with portions of the flow field where particle residence time is significantly elevated, such as areas of flow recirculation or oscillation. Coupled with increased endothelial permeability, locally increased residence time can enhance the mass transport into the vessel wall of both LDL and inflammatory cells at the lesion site [81]. Inside the intima, monocytes are activated to macrophages that phagocytize oxidized LDL; after extensive phagocytic activity the swollen macrophages take on a *foamy* appearance and are termed *foam cells.* It is the accumulation of foam cells, collagen, elastin, fibrin, extracellular cholesterol, and other cellular debris that forms an atheromatous plaque. The initiation and progression of atherosclerosis is strongly influenced by local biochemistry and cellular-level processes, and a comprehensive review is found in [104–106] and the references therein. For the present purpose, it will suffice to describe the structural aspects of the atherosclerotic vessel.

The earliest macro-scale manifestation of atherosclerosis is the presence of fatty streaks, which are caused by the accumulation of lipid-laden macrophages and

T-lymphocytes under the intimal endothelium [107]. At this stage, the atherosclerotic vessel has the mechanical response of the healthy vessel in a passive sense, although there may be a local decrease in nitric oxide (a vasodilator) production affecting its active response.

As atherosclerosis progresses, the arterial wall adopts a structure quite different from that of the healthy artery, and the mechanical response reflects this difference. Because atherosclerosis is a slowly progressing disease and its severity often correlates with advancing age, it should be noted that the aging intima thickens and becomes stiffer naturally [62]. Thus, in an atherosclerotic artery, even at locations without an acute plaque lesion, the intima can play a significant role in the mechanical response of the artery. This is in contrast to the healthy young intima, which does not have a significant impact on the structural mechanics of the arterial wall.

Earlier in the progression of a plaque, as foam cells accumulate in the intima, the vessel wall remodels and expands outward to preserve the patent lumen area [108]. Thus, the outer vessel wall may adopt a swollen appearance focally around the plaque and little or no luminal narrowing is present on an angiographic study. As the inflammatory response continues, SMCs are signaled to proliferate and are recruited from the media to the intima directly overlying the lipid and macrophage-rich plaque. These smooth muscle cells, and other fibrous components of the actively remodeling extracellular matrix constitute the *fibrous cap* of the plaque. It is the rupture or ulceration of this fibrous cap and subsequent exposure of highly thrombogenic plaque contents to flowing blood that can cause acute thromboembolic events like stroke and myocardial infarction [109]. A coarse view of the early atherosclerotic vessel would recognize the intima, fibrous cap, lipid and macrophage-rich plaque core, media, and the adventitia as distinct structural components with individual mechanical behavior. Of course, at the histological scale, each one of these components has a highly heterogeneous microstructure of its own.

Not every plaque ulceration or rupture will cause a thrombo-embolic event, and the disruption may eventually "heal" with the reformation of the fibrous cap. A series of ruptures and repairs can eventually lead to a large plaque that grows inward into the vessel lumen. Plaques with such a history are often the cause of high degree arterial stenosis, where the patent lumen diameter has been reduced by 50% or more [110]. These and other older plaques have a more irregular appearance and structure. The fibrous cap is of non-uniform thickness, and the lipid-rich plaque core has a very irregular shape and may not be a single continuous body. Additionally, bulk calcification and smaller calcium hydroxyapatite deposits are often present within surrounding fibrous plaque (regions of smooth muscle cells, collagen, and macrophages) and smooth muscle, and in the plaque core. The mechanical characteristics of the later stage atherosclerotic vessel are determined from the size, shape, strength and relative locations of the intima/fibrous cap, the remodeled media, the lipid-rich plaque core, fibrous plaque, calcification, and the adventitia.

The atherosclerotic artery wall is quite different from the healthy artery in both composition and mechanical response. In addition to the compositional and geometrical complexities of an atherosclerotic lesion, there are numerous ongoing biochemical processes that affect the mechanics of the lesion tissues. The cells

and materials present in atherosclerotic plaques play regulatory roles in these bio-chemical processes in addition to their structural roles, and thus the full mechanical characterization of a lesion is time dependent. Matrix metalloproteinases (MMPs) are expressed by various cells present in a lesion, and are capable of degrading structural proteins such as collagen and elastin. The MMPs are largely inflamma-tory mediated, and so the inflammatory state of the lesion and the macrophage and monocyte population of the tissues is thought to be of great importance to the like-lihood of mechanical failure.

11   Solid Mechanics of Idealized Plaque Lesions

Neglecting the ongoing biochemical changes in the active and inflamed plaque, the mechanical characteristics of the later stage atherosclerotic vessel are deter-mined from the size, shape, and relative locations of the intima/fibrous cap, the remodeled media, the lipid-rich plaque core, fibrous plaque, calcification, and the adventitia. The techniques used to perform computational analyses of these lesions are largely the same as those used to study a healthy vessel. The most notable dif-ferences are the requirements for further material characterization of lesion tissues, and for more advanced methods of mesh generation.

The general goals of computational mechanics investigations of atherosclerotic vessels are the understanding of lesion behavior and estimation of plaque rupture potential. Although there exist histological characterizations of plaques that are vul-nerable to rupture, it is still not exactly clear what the rupture mechanism is, nor what mechanical environment(s) leads to it. As previously discussed, the obvious system to study in atherogenesis investigations is the not-yet-diseased vessel. In much the same way, the obvious systems to model in studies of plaque rupture are vessels that contain unruptured and ruptured atherosclerotic lesions.

Because of the great variety of material shapes and distributions, several groups have constructed idealized models of atherosclerotic vessels. In this way, geometric characterization of the model is trivial, and stresses and strains are easily related to features such as fibrous cap thickness, lipid pool volume, calcification/lipid volume ratio, and lumen eccentricity. In [103], Loree et al constructed a 2-D model of an atherosclerotic coronary artery to investigate the effects of fibrous cap thickness on circumferential stress. This classic 2-D model was of a transverse cross section of an artery with an eccentric fibrous plaque burden and a crescent-shaped lipid pool, with hemi-circular ends, extending 140° concentric with the lumen. At the time of this study, little data on the nonlinear material properties of arterial tissue or fi-brous plaque existed. Because of this, linearly elastic, transversely isotropic material parameters measured in other published experiments were used. The Young's modu-lus in the radial direction was five times higher for fibrous plaque than for artery wall tissue, and the circumferential modulus and shear modulus were ten times greater for the fibrous plaque. The Young's modulus of the isotropic lipid was taken to be $1/100$ that of E_θ for the arterial tissue. Ten similar geometries of varying fibrous

cap thickness were meshed with eight-node quadrilateral plane-strain elements, and adaptive remeshing was employed through the simulations. The luminal surface of the atheromatous arterial mesh was subjected to a pressure load of 110 mmHg, and boundary conditions exploited symmetry. In a first study, the authors changed the fibrous cap thickness by varying the lipid pool thickness at constant stenotic severity, and found that the peak circumferential stress normalized by the luminal pressure increased significantly with decreasing cap thickness. At a cap thickness of 0.5 mm, the normalized stress was around 5, and rose nonlinearly to 25 at a cap thickness of 0.1 mm. Nearly identical stresses were found when varying the cap thickness by changing the stenosis severity at constant lipid pool thickness. When changing the stenosis severity in a model without a lipid pool, virtually no change in normalized peak stress was seen. Thus, the study showed that fibrous cap thickness, and not stenosis severity alone, was likely the dominant factor influencing plaque rupture risk, as fibrous plaque must experience mechanical failure at some level of stress.

The use of a plane strain finite element model by Loree et al was justified by the assumption that the plaque structures of interest would extend nearly a vessel diameter along the vessel axis. Such an assumption is reasonable for many analyses and is common in the literature, but careful attention must also be paid to the longitudinal distribution of stress in the diseased vessel. The material properties from [103] were used by Imoto et al. in [104] in studying the longitudinal distribution of von Mises stress in representative plaque/artery structures. Although the authors state that plane strain elements were used, their results show that the finite element formulation was axisymmetric to match the geometry. Plane strain elements would not have accurately accounted for the dominant circumferential component of stress. Imoto et al reported that there were stress concentrations at the "shoulders" of the plaques, the longitudinal positions where the plaque began and ended. This result cannot be seen in a transverse 2-D model. Peak stresses were higher, assuming constant thickness plaques, for geometries with positive remodeling as opposed to those with stenotic remodeling. For the models that included lipid pools, the authors reported that the cap stresses increase dramatically with decreasing cap thickness, in agreement with Loree et al. Referencing the literature, the study used a fibrous plaque yield strength of 300 kPa, and noted that this stress was exceeded when the fibrous cap over a lipid pool was thinner than 60–100 μm, depending on vessel radius. This finding agrees well with the critical cap thicknesses reported in several other studies. The size of the lipid pool was shown to have no effect on the peak stress in the cap directly overlying the pool, and calcification within the cap overlying the pool was shown to reduce cap stress magnitudes.

In [50], Tang et al investigated the effects of lipid pool size and cap thickness on the stress distributions in fully three-dimensional geometries using FSI to load the diseased artery wall model. Tang et al reported that the model with a smaller lipid pool and thicker cap than the baseline model experienced a peak stress reduction of about 20%, and that the same geometry without a lipid pool experienced a stress peak reduction of 33%. When the size of the lipid pool was greater than that of the baseline model, the stress peak increased by about 30%. The models used were for 100% eccentric plaques, and the stress peaks were all on the luminal surface

opposite the plaque, although the authors noted that a further reduction of cap thickness resulted in maximum stress at the thinnest point of the cap. As the lipid material was taken to be highly deformable, compressive stresses more than doubled when the lipid pool size was increased. Li et al [105] further investigated the deformation of an idealized dome-shaped, 100% eccentric plaque subjected to carotid artery-like flow conditions. In their longitudinal cross section model, fibrous cap thickness was varied between 0.1 mm and 2 mm, and 90 different stenotic severities between 10% and 90% were simulated. A two-term Ogden model was used to characterize both the fibrous cap and lipid pool. Due to the inlet pressure, and impinging flow, maximum deformation of the plaque was seen on the proximal edge of the plaque about midway from shoulder to peak stenosis. Maximum principal stress was highest at points surrounding maximum deformation, indicating a bending mode of deformation in the cap. Li et al's parameter study showed that for stenoses of 30–70%, plaque cap thickness was a critical determinant of rupture potential, using the often cited 300 kPa possible rupture stress [106]. For cap thicknesses of 100 μm or less, rupture was predicted for even 10% stenosis. Although their model was very simple, the authors noted that the stress distributions calculated correspond well with the proximal-surface ulcerations seen histologically in such lesions.

11.1 Microcalcifications

The work of Imoto et al [104], and studies by several other groups, showed that calcifications within the fibrous cap attenuated cap stress levels and therefore made rupture less likely. Additionally, the work of Huang et al. [107] showed that the there was no significant change in maximum principal stress when calcifications were replaced by fibrous plaque in the FEM models of 20 resected coronary arteries. This was in contrast to the sometimes-severe decrease in stress when a lipid pool was replaced with fibrous plaque in the models. The calcifications considered in this work were not specifically overlying any lipid pool present. In these studies the calcifications considered were large, on the order of the cap thickness or larger. In [108],Vengrenyuk hypothesized that smaller calcifications can actually induce fibrous cap rupture through a debonding process caused by significantly elevated interfacial stresses at the surface of the calcified inclusion. The theoretical solution presented in the paper was not specific to a vascular model, and was based on a single rigid spherical inclusion eccentrically located in a thin elastic layer (2–10 inclusion diameters) under uniaxial tension. The upper and lower surfaces of the elastic layer were considered stress-free. Results suggested that if an inclusion is present in a thin fibrous cap near the lipid-pool boundary, then a region of the cap that would be stressed above 300 kPa without the inclusion would see a local stress increase of nearly a factor of 2. The authors noted that this could explain the paradox that although plaque rupture is commonly seen at regions where high stress was predicted, the rupture point is not always at the point of maximum predicted stress. Microcalcifications are very small, on the order of 10 μm, and are not

detected by clinical imaging. For this reason, mathematical models of atherosclerotic plaque had not previously considered their effects. In addition to calculating the stress amplification due to such inclusions, Vengrenyuk et al. also used confocal fluorescence microscopy and micro-computed tomography to search for microcalcifications in resected coronary lesions. Although microcalcifications in the fibrous cap were found to be less common than calcifications in the necrotic core of the plaque, their presence may help explain why some plaques rupture where coarse resolution mechanics suggest they should not.

In [109, 110], Bluestein and Avrahami et al. studied the influence of microcalcifications in an idealized stenotic vessel similar to that in [50, 104, 105]. Two FSI models were constructed of ideal coronary arteries in [110], one with 80% stenosis severity by area, the other with 34% stenosis. The dimensions of the artery wall, lumen, and lipid pool are provided in the original paper, but it should be noted that minimum cap thicknesses were 40 and 60 μm for the more and less stenotic models, respectively. In this way, more realistic lesion geometries were considered, and the studies' results could be interpreted with those of [108] in mind. Full 3-D FSI simulations were run for each model with and without a 10 μm diameter spherical calcification placed mid-thickness within the fibrous cap. Each material present was modeled as a modified Mooney-Rivlin solid, with material parameters taken from [52]. A physiological coronary artery flowrate waveform with assumed parabolic profile was applied at the lumen inlet, and the outlet was considered traction free. The remaining boundary conditions, although common for such models, do not accurately capture the mechanical environment of the coronary arteries, which undergo cyclic compression from surrounding myocardium. The peak wall von Mises stresses were always on the proximal surface of the stenosis, and were nearly tripled when a calcified inclusion was modeled. The model with 80% stenosis experienced significantly higher stress magnitudes than the 30% case. In addition to the highly elevated stresses due to a calcified inclusion, the more and less stenotic models each saw a roughly 10% increase in first principal stretch when the inclusion was considered. This translates into a considerable difference in local strain.

12   2-D Patient-Specific Plaque Studies

As studies like [50, 103–105, 111] have shown, the stress and strain fields in the diseased arterial wall are strongly influenced by the shape and size of the lumen and other features like lipid pools, calcifications or fibrous plaque burden. Although these models have yielded much useful information about the mechanics of the atherosclerotic vessel, idealized geometries impose limitations on their utility. Studies on idealized diseased vessels cannot be used to investigate the mechanics of a real lesion, whose evolution *in vivo* may or may not be known. These studies are also not capable of relating the mechanical environment to biological factors like inflammatory state or histologically determined composition. Furthermore, such studies are incapable of establishing material parameters for real tissues using an

optimization or inverse-problem technique.[4] It is therefore of great interest to study the mechanics of the atherosclerotic vessel on a patient-specific basis, using geometries and compositions determined from histological analysis, or *in-* or *ex vivo* imaging methods.

Due to a lack of suitable non-invasive imaging techniques, the earliest patient-specific studies of atherosclerotic lesion mechanics used histological information to construct a finite element model. The possibility for specimen distortion and damage made this approach challenging for discerning the true *in vivo* state of the diseased vessel. Additionally, histological analysis requires a very thin slice of the tissue to be used, and thus these models were restricted to 2-D analyses that invariably assumed a plane-strain state of stress. While the plane-strain assumption is likely admissible for certain lesions, other lesions involving significant longitudinal variation in composition or boundary conditions may require a fully 3-D analysis. In [112], Cheng et al investigated their hypothesis that plaque rupture occurs at sites of elevated circumferential stress by performing finite element analyses of 24 coronary lesions. Twelve ruptured lesions from patients who died from coronary thrombosis, and twelve unruptured lesions from patients without thrombosis were used in the study. Contours were drawn for fibrous plaque, vessel wall, calcification, and lipid pool as determined histologically. The digitized contours were used to construct FEM meshes. Ruptured plaques were reconstructed into their probable pre-rupture states. All materials were assumed to be linearly elastic and transversely isotropic, using the same moduli and Poisson ratios as [103]; the Young's modulus of the calcified regions was taken to be tenfold that of E_θ for fibrous plaque. The luminal surfaces of the models were loaded with a pressure of 110 mmHg. Cheng et al found that 12 out of 12 ruptured lesions had a combined 31 regions of circumferential stress exceeding 300 kPa, while only one stable lesion demonstrated one area of such elevated stress. Furthermore, the authors found that 7 out of 12 ruptured lesions ruptured at the area of peak stress, and ten out of 12 ruptured at regions where stress exceeded 300 kPa. The average calculated peak stress in ruptured lesions was significantly almost 2.8 times higher than in the stable control lesions. These results indicated that elevated circumferential stress may indeed contribute to plaque rupture in the coronary arteries.

In [113, 114], Kaazempur-Mofrad and Patel et al also employed FEM models built from histological data. In [114], the authors investigated the correlation between various mechanical descriptors and histological findings for unruptured plaques freshly harvested at carotid endarterectomy. The transverse slices of diseased vessel were cut radially so that they could assume their macroscopically stress-free state. Histological staining for collagen, smooth muscle cells, lipids, and macrophages allowed delineation between arterial wall tissue, fibrous plaque, calcification, and lipid pool. The histologically determined segmentation of each component was used to construct a finite element mesh of the artery in the stress-free state. Plaque components and arterial wall were all modeled as Mooney-Rivlin

---

[4] See the 'Current Developments' section at the end of this chapter.

rubber-like solids, and the segmented geometries were discretized using nine-node plane strain quadrilateral elements. Thermally contracting truss elements were used to rejoin the cut ends of the unstressed vessel wall, and thus residual strains and stresses were approximated for the diseased vessel models. After the thermal load was applied to rejoin the cut ends of the section, the luminal surface of the diseased vessels were loaded with patient-specific diastolic and systolic pressures, as measured prior to surgery. von Mises stress, circumferential stress, and cyclic strain were calculated for each specimen. Significant negative correlations were found for both collagen and macrophage content and the mechanical descriptors at the luminal surface averaged over 15° circumferential sectors. No significant correlation could be made for lipid or smooth muscle cell content. The most significant correlations were made with respect to cyclic strain, indicating that this descriptor should not be overlooked when trying to establish rupture risk, as it is may be most indicative of an active remodeling plaque. The authors demonstrated, in [113], that cyclic strain was virtually identical whether or not the residual stresses were incorporated via the thermally contracting truss scheme. This is an important result, as studies like [115] by Ohayon et al show that residual stresses can still be quite significant in heavily diseased coronary vessels. In that study, the authors used histological staining to define the boundaries between vessel wall, fibrous plaque, and lipid pool. The geometry was meshed using six and eight node plane strain elements, and the materials were all represented as neo-Hookean solids. The cut ends of the stress-free open sector vessel walls were rejoined to determine the residual stresses and strains. After the segments were closed, and thus residually stressed, a pressure load of 16 kPa (120 mmHg) was imparted to the luminal surface of the model. Incorporation of residual strains was shown to reduce calculated peak stresses, sometimes by roughly a factor or 4. Additionally, accounting for residual stresses lead to quite different von Mises stress fields, with new stress peaks away from the luminal surface, or even behind a lipid pool in some cases. Thus, the importance of residual stresses should be established on a case-by-case basis to ensure the most accurate stress and strain calculations.

Other studies, such as [111], have investigated the cyclic straining of the tissue of a plaque lesion, and its implications on fatigue modes of failure. In [111], Versluis et al used an idealized model similar to that in [103], with materials modeled by a two-term Ogden strain energy function. A crack propagation algorithm using a modified Paris relation was employed to determine the progressive fracture in the lesion based on evolving stress fields. While there are still many uncertainties in the fracture mechanics of fibrous plaque tissue, the study yielded several interesting results. Cracks were seen to propagate nearly radially from the initiation point, a point of peak stress, so initial stress distributions may be suitable for prediction of a fracture path. Also, reduction of heart rate, mean and pulse pressure, and a reduction in stiffness disparity between plaque components were shown to increase time to rupture in the evolution models.

As previously mentioned, histological analysis necessitates that the tissue be prepared and sectioned into very thin slices, often 5 or 10 μm. Tissue preparation can lead to non-uniform desiccation and shrinkage, and handling can easily result in

tears and other tissue distortions. Using histological data to construct an FEM model that accurately represents the diseased vessel without artifacts can be difficult. Citing limited resolution in other non-invasive imaging modalities, Chau et al [116] used optical coherence tomography (OCT) to construct FEM models of diseased coronary arteries. OCT is an optical analogue to B-mode ultrasound relying on tissues' differential interactions with infrared light. OCT is capable of an in-plane resolution of tens of microns, and has been shown to accurately image the structure and composition of diseased vessel walls. In [116], the authors used segmented *ex vivo* OCT and histological images to construct two 2-D, plane strain FEM models of the same vessel at the same axial location. All vessel and plaque materials were modeled with the Mooney-Rivlin strain energy density function given in Eq. (9), with material parameters as in [86, 98, 99, 113, 114]. The diseased vessel geometries as identified by OCT and histology were slightly different in each case modeled, and the tissue boundaries identified at histological analysis were generally more irregular and jagged than those imaged using OCT. Each model was loaded with a luminal pressure of 0–120 mmHg in 5 mmHg increments. The computed von Mises stress and cyclic strain bandplots for each model were divided into 50 angular sectors so that the OCT and histology based models could be compared in a systematic way. Overall, there was good agreement between the two models, but the histology based models showed much higher peak stresses in the regions of high luminal edge curvature. Many of those stress peaks occurred at regions of the vessel where tissue handling caused reconstruction artifacts and sharp features in the FEM mesh. Unfortunately, the imaging penetration depth for OCT is limited, and imaging of diseased vessels can sometimes not fully resolve adventitial level features. To understand the implication of this on the calculated stress and strain fields, the authors used alternative segmentations of the same OCT data to build different FEM simulations. While there were certainly some sharp differences in segmented geometries, the overall stress and strain distributions were remarkably similar, and stress and strain results were least-affected at the luminal surface, which is of greatest interest. The authors concluded that OCT showed promise as an imaging tool for the construction of FEM models of diseased arteries.

OCT and intravascular ultrasound (IVUS) are both capable of imaging vessel wall structure and composition, and both have been used to study plaque mechanics on a patient-specific basis. The application of these imaging modalities is, however, not without challenge. Both OCT and IVUS require catheterization of the patient, and like any invasive procedure this carries some amount of risk. As mentioned, OCT has a limited penetration depth and may not be suitable for the study of larger, or more heavily diseased vessels. Although IVUS is often used clinically to investigate vascular structures, its ability to discriminate between soft tissues is somewhat lacking and may not resolve tissue boundaries adequately for FEM modeling. Additionally, each modality requires an automated pullback technique to scan the vessel longitudinally. Motion of the catheter within the vessel during pullback introduces significant difficulty in the reconstruction process, and advanced image registration is thus necessary for 3-D modeling. Although not exclusive to these modalities, vessel motion through the cardiac cycle, especially in the coronary arteries, also presents serious challenges.

Several groups have used MRI data to construct patient-specific FEM simulations of the atherosclerotic vessel. Li et al [117] used multi-sequence MRI to image diseased carotid arteries in five patients, and constructed 2-D FEM models based on the axially acquired images to study plaque rupture. 2-D black-blood spin echo sequences with intermediate T2 weighting and fat saturation, T2 weighting, T1 weighting, and STIR preparation were used to image lipid pool, fibrous cap, and vessel wall [118, 119]. Image resolution was $0.39 \times 0.39 \times 3$ mm. The characteristic appearances of these tissue types in the various imaging sequences allowed for a manual delineation between important plaque features. The assignment of tissue types was verified by histology on the same plaques after carotid endarterectomy. Control vertices from the manual segmentation were imported into a FEM preprocessor and used to define a set of closed B-spline areas suitable for mesh generation. Of the five plaques studied, two were ruptured as verified by MRI and histology, and three were intact. FEM meshes for the ruptured plaques represented their probable pre-rupture states. All materials were modeled with a two-term Ogden formulation, and material parameters were taken from earlier studies. A mean pressure of 115 mmHg was applied to the luminal surface of all models. The models of unruptured plaques predicted an average maximum von Mises stress of 226.9 kPa, whereas the models of ruptured plaques showed an average maximum stress roughly three times greater. To test the reproducibility of the method, two investigators independently segmented and modeled plaques based on the same 12 MRI studies. A Pearson correlation coefficient of 0.83 between computed maximum von Mises stresses suggested that individual error in segmentation and modeling likely influenced results to only a small degree. The results of the study suggest that maximal effective stress, influenced primarily by thinness of the fibrous cap and disparity between plaque and lipid stiffness, may be related to risk of rupture in carotid plaques. While this was not a new result from FEM modeling of atherosclerotic plaques, the study's use of actual plaque morphologies from *in vivo* MRI effectively introduced a new method by which plaque mechanics could be studied.

The same group extended their work by modeling the carotid plaques of 30 patients, 15 of whom had recently experienced a transient ischemic attack attributed to their carotid disease [55]. Using the techniques described in [117], FEM models were built for the symptomatic and asymptomatic patients, whose baseline risk factors and disease features were well matched. FEM mesh generation and analysis was performed independently from image acquisition and segmentation to avoid biasing of results. The symptomatic group showed a significantly higher maximal effective stress than the asymptomatic group, 508.2 ± 193.1 vs 269.6 ± 107.9 kPa (95% confidence interval of the difference was 121.7–355.6 kPa, P = .004). Similarly, Tang et al used *ex vivo* MRI as the basis for FEM models of 2-D transverse cross sections of 11 diseased coronary arteries [53]. The plaque specimens were classified by pathology on a 0–5 scale of rupture vulnerability, and a correlation between the classification and maximum principal stress was investigated. The data suggested a significant correlation between maximum principal stress and vulnerability, but the authors noted that a more comprehensive and large-scale patient study was needed to verify the patterns observed. The results of these studies suggest that stratifying carotid disease patients into risk groups based on careful biomechanical analysis may someday be of clinical utility.

Noting the Lovett and Rothwell's observation that carotid plaques were more likely to ulcerate proximal to the site of maximal stenosis [120], Kock et al [121] used *in vivo* MRI and FEM modeling to investigate the longitudinal stress distributions in two patients with symptomatic carotid stenosis. Axial T1W, T2W, PDW, and TOF images were acquired at resolution of $0.6 \times 0.6 \times 2$ mm. As all imaging studies were made with axial orientation and the FEM models were of longitudinal slices through the diseased carotid bifurcation, significant image processing and geometry preparation was necessary. Resampling of the raw imaging data using linear interpolation allowed a final isotropic voxel edge length of 0.3125 mm. Spline contours for all plaque components and vessel wall were made at each 2-D imaging slice and combined into 3-D sets of voxels representing different materials. The voxel sets were smoothed and used to define 3-D isosurfaces of each plaque component, and a full 3-D multicomponent representation of the diseased bifurcation was realized. A 3-D skeletonization of the vessel lumen allowed the authors to define a NURBS cutplane through an effective center of the 3-D model, and the intersection of the 3-D isosurfaces model and the NURBS cutplane established the geometry of the longitudinal 2-D model. As the final models were of longitudinal cross sections, a lumen remained through which blood flow could be modeled and FSI simulations were made. The meshed FSI model of the bifurcation was surrounded by a block of additional mesh that represented surrounding tissue. All solids were considered neo-Hookean, and blood was considered Newtonian. The material properties for the surrounding tissue were tuned so that vessel dilation at the proximal common carotid under systolic and diastolic pressure matched the deformation measured with a balanced TFE MR sequence. In effect, this radial constraint replaces the constraints caused by the natural tubular structure of an artery. Flow boundary conditions in the dynamic simulations were established through PC-MRI of the ICA, ECA, and CCA 2 cm proximal and distal to the apex of the bifurcation. While the models showed clear first principal stress peaks of reasonable magnitude proximal to the stenotic throat, interpretation of these stresses must be made carefully. It is not clear that the actual stresses in the artery are represented. A real artery would exhibit maximal stress in the circumferential direction, a state of stress not resolvable with this model. From earlier work [122] it is assumed that plane strain elements were used to account for an extended geometry, but it is not clear how well this approximation would hold for such geometry and loading. Kock et al's model, nonetheless, represents a comprehensive approach to constructing an FEM model of the carotid bifurcation from *in vivo* MRI studies, and contains nearly all salient modeling techniques used for fully 3-D simulations.

13 3-D Patient-Specific Plaque Studies

While 2-D analyses of diseased vessels have helped to identify relationships between morphological features and distributions of stress and strain, the *in vivo* mechanical state of the vessel is fully three-dimensional. 2-D studies of transverse

cross sections of the diseased vessel make a plane strain assumption, which may not be suitable for lesions whose longitudinal extent is limited. These models also fail to resolve out of plane components of deformation, which may be important for some lesions, depending on local composition and *in vivo* axial stretch. Furthermore, as shown in [49, 50, 75, 77], the pressure load felt at a longitudinal position in a diseased vessel is highly dependent on local geometry and flow conditions. Because of this, it is difficult to be certain that using systolic pressure loading at the luminal boundary of the vessel is appropriate in the 2-D model. Because of these limitations, several groups have begun to model diseased arteries using multicomponent 3-D FEM simulations, with either uniform pressure or strongly coupled FSI to effect vessel loading. There are numerous challenges in 3-D modeling of diseased vessels. Suitable imaging, image processing and segmentation is difficult to achieve. Mesh generation for complex 3-D geometries is tedious and mesh independence is not easily established. Additionally, nonlinear material response and strong FSI lead to convergence issues and high computational expense. For these reasons, 3-D multicomponent models of atherosclerotic vessels are relatively few in the literature compared to 2-D studies. Advances in imaging and FEM techniques, and the creativity of the groups making such models have allowed these challenges to be increasingly overcome, and the state-of-the-art is progressing rapidly.

In [53], Tang et al. used high resolution *ex vivo* MRI of a carotid endarterectomy specimen as the basis for their 3-D FSI model. Sixty-four slices at a resolution of $0.1 \times 0.1 \times 0.5$ mm were segmented into fibrous plaque and lipid pool; there was no calcification in the specimen. A constant 0.8 mm thick layer was added around the segmented geometry to account for the portion of vessel left behind at endarterectomy. The control points from the segmentation contours were used directly in the FEM preprocessor to construct volumes on which a mesh could be generated. No distinction was made in the computational mesh between fibrous plaque and vessel wall, and all solids were represented with a Moony-Rivlin material formulation. The vessel wall contours were extruded several centimeters at the ends of the 3.2 cm long segment imaged, providing extensions in which entering flow could develop and post-stenotic flow could return to being unidirectional. Constructing a computational mesh on which fluid and solid solutions can both converge, without the computation becoming prohibitively expensive, is a challenging task. While several variations were modeled to examine the relative effects of various parameters, the baseline model used normal tractions of 100 mmHg and 98.5 mmHg at the inlet and outlet of the flow domain, respectively, for a physiological carotid flow rate of 17.5 ml/s. An axial stretch of 20% was applied to the solid domain (the flow domain follows due to FSI boundary conditions) to simulate a reasonable *in vivo* condition. The study showed that the stresses and strains in the diseased vessel wall under physiological conditions are indeed highly three dimensional, and dependent on several factors. The flow boundary conditions and assumed state of axial stretch were shown to greatly affect the stresses and strains in the wall. Figure 9 compares the results obtained at the same location using 2-D and 3-D models with and without FSI and with varying axial stretches (Fig. 9).
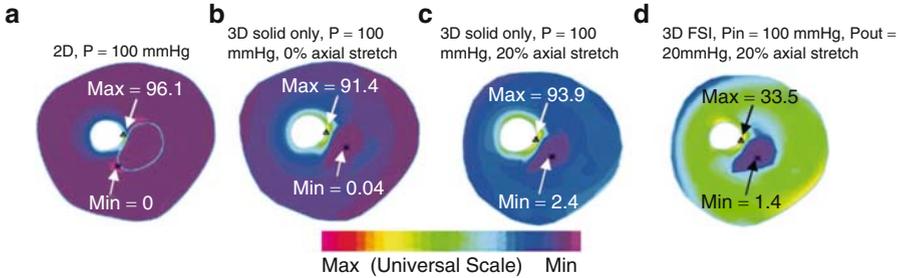
Fig. 9 (**a**) 2-D, solid-only model with plane-strain assumption; (**b**) Fully 3-D solid-only model without axial stretch; (**c**) 3-D solid-only model with axial stretch of 1.2; (**d**) Full 3-D, FSI model with pressure conditions at inlet and outlet for physiological flow rate, axial stretch of 1.2 (Taken from [53])

In the solid only results shown in Fig. 9a, b, c the benefit of the 3-D modeling and of modeling axial stretch is minimal, as the heavily diseased wall is quite stiff and resists longitudinal deformations. The differences between models a and d, however, clearly make a strong case for needing 3-D FSI simulations for stenotic geometries.

As many patient-specific 2-D and 3-D studies of plaque mechanics have indicated, the point of maximum stress is often at a relatively healthy region of the vessel. This indicates that simply noting the position of the global stress maximum does not equate to identifying the region of highest rupture potential. Citing this apparent shortcoming in the conclusions of the literature, Tang et al sought to develop a rupture risk assessment strategy based upon local stress characteristics [52, 123]. The general strategy is to use the accumulating knowledge of radiologists, pathologists, and medical scientists to select a number of "critical sites" at which various measures of stress are tracked through a dynamic 3-D FEM simulation based on *in vivo* MRI data. A database of FEM models and corresponding histopathological characterizations of the same plaques is used to define an ordinal multinomial general linear model that relates measures of stress at critical sites to a validated histological scale. In this way, the vast amount of data generated in an extremely realistic dynamic 3-D FEM simulation can be pared down to stress information local to regions of interest and this information can suggest a plaque vulnerability index. Tang et al's critical site selection criteria are still evolving and the idea shows promise in giving clinical utility to the complex and powerful MRI-based 3-D FSI modeling techniques used in [51–53, 123, 124].

More recently, Tang et al. have used their 2-D/3-D FEM techniques to study plaque progression as opposed to plaque rupture [51]. Although it is generally accepted that atherogenesis occurs at regions of low or oscillatory wall shear stress, it is not understood why more advanced plaques in high wall shear stress environments continue to develop. Tang et al tested their hypothesis that plaque progression, as measured by a wall thickness increase, is correlated to mechanical stresses within the plaque. The study was actually conducted using 2-D FEM models, but a 3-D FSI model was used for validation purposes. In the study, 20 patients were imaged

at baseline and after 18 months, one patient received a follow-up MRI study at 10 months. The MRI datasets were used to construct 2-D FEM models of several axial locations at each time point. Because MRI data is acquired at systemic pressure, when the vessel is dilated, a shrink-expand approach was taken in the modeling. A scaling factor was determined for each case such that the scaled down model's lumen would match imaging data when the model was subjected to luminal pressure. The typical shrinking factor was 8–10%. Wall thickness was measured as the shortest distance between a luminal node and the outer wall boundary. Three hundred to seven hundred luminal points at several axial locations were tracked for each patient at baseline and follow-up, and wall thickness, wall thickness increase, and maximum principal stress were recorded. The authors report that a statistically significant negative correlation was found between wall thickness increase and maximum principal stress (measured at the later time point) for 18 of 21 patients. Using a 3-D FSI model, the authors also showed that wall thickness increase was negatively correlated with maximum flow shear stress. While the regression analyses between wall thickness increase and maximum principal stress and flow shear stress individually achieved an R^2 of roughly 0.27, a multiple regression analysis of thickness increase to both wall stress and flow shear stress achieved an R^2 of 0.637. The analysis attempted is quite difficult for many reasons, not least of which are the uncertainty of segmentation and the complicated effects of the shrink-expand technique. It is hoped that with more data, and more experience, this type of work will allow for a prediction of plaque progression that can be used clinically for some benefit. Tang et al are continuing to gather longitudinal patient data so that a greater number of more comprehensive 3-D FSI analyses can be made.

13.1   Plaque Lesion Fracture, Dissection, Stenting, and Angioplasty

Most of the 3-D patient-specific studies in the literature focus on quantifying the stresses and strains in the diseased vessel, admitting elastic deformation but neglecting permanent changes to the structure and mechanical response of the materials. In contrast, very few studies explicitly consider inelastic effects, for which experimental data and constitutive relations have traditionally been sparse. More recent developments in constitutive modeling and finite element methods have allowed researchers to investigate plaque rupture, arterial dissection, and inelastic deformation of the diseased vascular wall. Investigations have increasingly been made on patient-specific geometries as determined with MRI. It is hoped that such work will elucidate the critical mechanics of surgical interventions like stenting and balloon angioplasty, as well plaque ruptures that may occur during a lesion's natural evolution. Such knowledge would be useful in designing optimal interventional devices and procedures, perhaps on a lesion-specific basis, and for the determination of medical therapeutics that influence either plaque mechanics or the arterial mechanical environment. Furthermore, detailed knowledge of the mechanical and material

changes that follow controlled vessel injury from balloon angioplasty or forced luminal patency from stenting could shed light on the primary factors influencing vessel restenosis, an unfortunately common occurrence after such treatments.

In [125], Holzapfel et al used high resolution *ex vivo* MRI ($0.3 \times 0.3 \times 1.0$ mm) to determine the structure and composition of a diseased segment of an external iliac artery. The imaging data was used to construct a lesion-specific FEM model to investigate the arterial stresses before, during, and after balloon angioplasty. After imaging, the arterial segment was cut longitudinally into two halves. One half was examined histologically to make a detailed determination of the tissue types found in the lesion. The tissues of the other half were carefully dissected from each other and subjected to mechanical testing. In this way, the MRI data could be used to accurately define the distribution of tissue types and their specific material responses. In all, 8 different tissues were distinguished in the diseased vessel and represented geometrically with NURBS surfaces. Various regions (diseased and not) of the intima, media, and adventitia were all modeled using the fiber reinforced composite constitutive model presented in [21], with parameters determined from fitting to the testing data. The non-diseased media and intima were modeled using an elastoplastic adaptation of the same constitutive relation, as given in [61]; the non-diseased media was the only tissue to exhibit non-recoverable deformation during testing, and the intima behaves as fully plastic past its yield strength to easily capture damage-like effects. The finite element equations, using a three-field variational principle to handle incompressibility, were solved over a structured mesh of eight node hexahedra. The fully inflated balloon was modeled as a 10 mm diameter rigid cylinder, which is admissible based on experimental observations. An axial stretch of 1.04 was applied to all material layers except the adventitia, on which a stretch of 1.2 was applied to match experimental observation of the specimen. A luminal pressure of 100 mmHg was applied in all cases. At full balloon dilation, the elastic limits of the non-diseased intima and media were exceeded, causing non-recoverable deformation that resulted in a significant luminal gain post-angioplasty. This also indicates that damage or fracture of the intimal surface is likely during the procedure. The medial deformation fits well the clinical observation that it is the overstretching of remnant healthy tissue that gives angioplasty therapeutic efficacy.

Post-angioplasty stresses are quite different than those at systemic pressure before balloon expansion. The distribution of stress differences is complicated, and depends heavily on the extent of plastic deformation, the relative volumes of plaque materials, and their arrangement. The inelastic deformation of the healthy intimal tissue led to a moderate stress relief there as well as in abutting tissue layers, while the fibrous intimal tissue at the medial border experienced a 50–60 kPa stress elevation. Such changes in the mechanical environment of the vessel may be the stimuli to which the vessel biologically responds, and thus may be related to occurrence of restenosis. A comparison was made between the baseline results at full balloon dilation, and stress fields calculated under simplifying assumptions commonly found in the literature. Figure 5 in [125] displays the differences, and demonstrates that assumptions of material isotropy, or plane strain mechanics do not accurately predict stress fields in such a heterogeneous specimen under supraphysiologic loading.

This is also suggested in the more general findings of [126], in which an idealized and simplified lesion was modeled under therapeutic loading. Although idealized, the diseased vessel model studied by Gasser et al. in [126] was more realistic in the specific sense that it included residual circumferential stresses. As discussed earlier in this chapter, residual stresses can have a significant impact on the total state of stress in the vessel. It is not clear how to best determine these stresses in heavily diseased vessels, so the patient-specific study left them out. Neglecting to account for *in vivo* axial stretch was also shown to have a deleterious effect on stress predictions, most notably in the non-diseased portions of the wall.

In [127], Gasser et al. continued to study the mechanics of balloon angioplasty in heavily diseased vessels, this time explicitly modeling fissuring and dissection of the plaque. Their earlier work focused on a fibrotic and calcified plaque, and plasticity theory was used to model the non-recoverable deformation observed. In this study however, the focus was a lipid-rich plaque, and the deformation and damage mechanisms of such lesions are clinically seen to be different. Informed by the recent experimental work of Sommer et al [128] and their recent modeling of arterial dissection [129], the authors used a cohesive zone formulation and the partition of unity finite element method and interface element method to represent fissuring and dissection of the tissues. The vessel segment studied was from an external iliac artery with a lipid-rich plaque lesion. High resolution *ex vivo* MRI was used to delineate the major tissue types of the diseased vessel, and a 3-D reconstruction was made based on the methods in [130]. An unstructured tetrahedral mesh was generated separately for each tissue component, and the interface element method was used to link boundary surfaces of different components. The authors applied a transformation to the patient-specific geometry mapping it to an eccentric thick-walled tube, allowing easy specification of material axes. A pull-back operation on these axes into the true irregular reference geometry allowed the use of the anisotropic fiber reinforced composite constitutive relation developed in [3]. Material and structural parameters were determined through mechanical testing of lesion tissues, as documented in [125]. At a balloon diameter of 3.52 mm, which represents a significant expansion of the rather stenotic lumen, maximum principal stresses of roughly 500 kPa are seen at the shoulders of the lesion. An intimal fissure also developed at the shoulder where the fibrous cap was thinner; until the fissure developed, the media and adventitia were shielded from stress. In the continuation of this first stage of failure, fissuring also occurred at the other shoulder, and the load then caused elevated stresses in the media and adventitia. During a second stage of failure, the intimal layer dissected from the media at the level of the internal elastic lamina at the shoulders of the plaque. The authors note that the dissections prevented stress elevations throughout the lesion, and kept damage local to the dissection sites.

Similar tissue damage patterns were seen in the results of Ferrara and Pandolfi's models [131, 132]. In [131], a stenotic artery of unspecified origin was imaged *in vitro* using MRI, and a three-layer vessel geometry was constructed with a lipid pool within the thickened intimal layer. The geometry was meshed in an unstructured fashion using higher-order tetrahedral elements. After an axial stretch of 1.2, the luminal surface of the model was subjected to a maximum pressure of

260 mmHg. The authors represented the arterial tissues using the material formulation of Holzapfel, Gasser, and Ogden [21], with material parameters from [133]. Similar to [127], the authors chose to capture damage phenomena with the use of a cohesive surface formulation as opposed to a sharp crack tip model. In light of the histological evidence of fiber bridging in [128] and elsewhere, this seems appropriate. Ferrara and Pandolfi's model shows cracks in the intimal surface that propagate radially, in agreement with the 2-D fatigue models in [111].

Unlike [129] and [127], where an isotropic cohesive zone model is employed to handle tissue damage, Ferrara and Pandolfi's model utilizes an anisotropic cohesive theory in which material anisotropy gives an ellipsoidal resistance surface, and directional scaling applies to the traction axis. Experimental evidence [134] suggests that shear stresses also play a role in tissue damage. Neither Gasser et al, nor Ferrara and Pandolfi were able to incorporate this observation in their cohesive zone models however, as there is currently a lack of data characterizing such failure modes. In fact, as discussed in [127], data are lacking concerning the shape of the cohesive law, and fracture energy for arterial tissues, and thus the softening region of material behavior is still largely approximated.

13.2 Stenting

The literature on stenting is extensive, and models of stent placement have been conducted in 2-D and 3-D idealized and realistic vessels. As a majority of vascular stents are placed with a balloon catheter during angioplasty, the considerations of stent placement modeling are largely the same as those for modeling angioplasty, and the effects of common modeling simplifications are similar. Some stents are placed directly after a balloon angioplasty procedure or are self-expanding, and thus the details of modeling the placement and action of the stent may be different. From a mechanical point of view, the additional challenges in modeling balloon expandable stent placement are the complex multi-body contact problem wherein balloon, stent, and diseased vessel may all interact, and the resolution of arterial stress fields local to the stent struts. Detailed knowledge of the arterial damage and focal stresses resulting from stent expansion and placement can help to reveal the mechanical stimuli for the biological responses that lead to in-stent restenosis. Such knowledge will additionally inform the design of better stenting procedures and stents themselves, perhaps on a lesion-specific basis.

The literature contains many studies that focus on finite element-aided optimization of stent design. Such works are concerned primarily with expansion dynamics, plastic deformation, compression behavior, and failure/fatigue risk. These issues are mainly influenced by the materials used for stent construction, and the geometrical design of the particular stent, which are design variables; loading is often considered only generically. In contrast, studies focused on the arterial mechanics of stent placement must not only accurately model the stent and any deployment device, but must also fully consider the arterial structure and response, and the interaction

between vessel and stent. While no study has yet succeeded in modeling all aspects of balloon, stent, artery, and their interactions simultaneously at the state of the art, several studies serve as landmarks of modeling progress in the field.

In [125], Holzapfel et al, in addition to studying the mechanics of angioplasty, investigated the arterial stresses resulting from stent deployment in a human externl iliac artery. The arterial model's geometry and material properties were among the most realistic considered in a stenting study. MRI and histology were used to define the geometrical arrangement of eight different tissue types, and mechanical testing of the tissue provided material parameters to the advanced constitutive relation of [21]. Plastic deformation was modeled to capture the effects of tissue damage from the supraphysiological loading in a phenomenological sense. The study considered the deployment of a *Palmaz-Schatz* stent, with material properties consistent with a 316L stainless steel construction. The stent structure was modeled with three-node beam elements using a hybrid formulation. The discretization of the diseased artery was not sufficiently fine to resolve local stress patterns around the cells of the stent, and only bulk stress and strain fields were obtained in the study. Placement of the stent caused high circumferential tensile stresses in the non-diseased intima near the longitudinal boundaries of the device, with *compressive* axial stresses. The adventitial axial stresses were noted to be tensile at this longitudinal position, indicating that the stress state is indeed complex and three-dimensional. In this study, no attempt was made to model the balloon catheter used to expand the stent, and the complex contact problem was avoided.

Citing the lack of complete models in the literature, Liang et al. modeled the entire stent deployment system in [135]. The model contained representations of the balloon, stent, coronary artery wall, and a layer of plaque material affixed to the luminal surface of the idealized artery. The mechanical response of the balloon during inflation was modeled in two distinct phases to represent the relatively easy initial inflation and the stiffer response after reaching its original diameter of 2.8 mm. The balloon was discretized as a cylindrical surface of four-node shell elements. The open-cell stent with "V" hinges was discretized using 20-node brick elements, as was the cylindrical layer of plaque material. The artery was modeled with a hyperelastic material formulation and its cylindrical geometry was meshed with eight-node brick elements capable of large deformation analysis. A viscoplastic material formulation was used for the plaque material to achieve non-recoverable deformation and prevent 100% elastic recoil. Fifteen atom of pressure was applied to the inner balloon surface, and the lumen of the stenotic artery was expanded from 1.5 mm to 3.5 mm. After balloon deflation, a recoil of 12.3% by diameter was observed, which was roughly half the recoil of a similar angioplasty-only simulation performed. At the completion of stent placement, high stresses ($\sim$5.5 MPa) in the plaque were observed along the stent struts, and maximum stresses (on the order of 8 MPa) were seen where the "V" hinges between cells contacted the plaque surface. These stresses are extremely elevated, no doubt due to the lack of inelastic deformation of the arterial tissue and hence overstated recoil.

A similar analysis was made by Lally et al. in [136]. In this study, arterial wall stresses were calculated after deployment of Medtronic's S7 stent and Boston

Scientific's (REF) NIR stent into an axisymmetric stenotic coronary artery with a crescent-shaped plaque. The material formulation used for the arterial tissue was a five-term Mooney-Rivlin model, with parameters fit to femoral artery experimental data from an earlier study. The plaque was assumed to be mainly calcified, and was also modeled using the five-term Mooney-Rivlin formulation, with parameters taken from the literature. The stent was modeled as linearly elastic 316L stainless steel, without plastic deformation. An axial stretch of 1.2 was applied to the arterial mesh to approximate *in vivo* conditions. The balloon catheter deployment system was not modeled, and the loading scheme used was rather interesting. First, a pressure load of 13 MPa was applied to the hyperelastic artery, with the stent nodes inactivated in the system matrix through the element "birth – death" feature in the commercial FEM package. Then, the pressure load on the artery's luminal surface was incrementally reduced back to 13.3 kPa (100 mmHg) with the (fully expanded) stent nodes activated in the system matrix, and the contact problem was solved. The stent and artery/plaque surfaces were modeled using NURBS, and thus a stable contact scenario existed, where contact surface normals vary smoothly over the meshes. The high quality meshes used for the stent models and for the artery and plaque, and the automatic remeshing algorithm employed allowed a detailed resolution of contact stresses throughout the model, and a calculation of stent/tissue contact area. For the NIR stent, contact area was calculated as $13.9 \, \text{mm}^2$, with 21% of the stented artery experiencing stresses of 4 MPa or greater. The S7 stent contacted $11.3 \, \text{mm}^2$ of the diseased vessel, and imparted 4 MPa or greater stresses to only 4% of the vessel. Although the lack of tissue damage and non-recoverable stent deformation certainly effect the accuracy of the stress predictions, the study is useful on a comparative basis and may help explain why the clinically observed restenosis rates for the NIR and S7 stents are 19% and 10% at 6 month follow-up, respectively [137, 138].

In [139], Kiousis et al made what is likely the most accurate and detailed study on stent deployment to date. The geometry of a diseased external iliac artery was obtained using *ex vivo* MRI, and tissue distributions and material properties were taken from a prior angioplasty study by Gasser et al [127]. The parallel-fiber limiting case of the material formulation given in [3] was used to represent all arterial tissues in this work. Three stents, Boston Scientific Sverige AB's *Express Vascular LD,* and two parametric variations on that design, were modeled in this study; all stents were discretized using two-node large displacement, large rotation frame elements. The stents were all modeled as being 316L stainless steel using a combined neo-Hookean/von-Mises-Hill plasticity model. The material response of the balloon is highly anisotropic and nonlinear, and a special material formulation developed by the authors [140] was employed. This formulation is based on fiber-reinforced composites, and while not a realistic depiction of the balloon's material structure, it is capable of capturing well the balloon's mechanical response. As noted in [136] and discussed in this work, smooth analytical contact surfaces allow a greater stability and accuracy in the solutions of contact problems. For this reason, the contact surfaces in this work's node-to-surface contact strategy are represented as uniform cubic B-spline surfaces, constructed as documented in [140]. This method affords

C^2-continuity at surface borders, but necessitates the use of a structured grid with quadrilateral faces, thus mesh generation for realistic arteries becomes slightly more challenging. The stent, artery, and balloon were all allowed to contact each other. While tissue damage is not explicitly modeled in this work, the results of the previous angioplasty study of this geometry [127] show that the intima will fissure and dissect from the media at the shoulders of the plaque lesion. Two intimal tears consistent with these results are placed within the model geometry so that accurate stress calculations can be achieved without directly modeling damage. The balloon catheter and stent are placed into the arterial model with penetration of the meshes, and an incremental increase of the contact penalty parameter brings the system to equilibrium where the stent/balloon just contact the luminal surface. An increasing pressure load is applied to the inner surface of the balloon and the contact problem is solved incrementally until the balloon outer diameter is 4.5 mm (at about eight bar), at which point the balloon contact penalty parameter is reduced to simulate deflation.

Three stent geometries were considered in [139], the *Express Vascular LD* (hereafter, "factory stent") as it is manufactured, a variant with ∼29% thinner struts, and a variant with seven struts circumferentially as opposed to the standard 15. All loading and boundary conditions were the same for each case. The authors reported their results in a clinically relevant manner as a trio of scalars, D_1, D_2, and LG, for each stenting case and an angioplasty-only case. D_1 is a measure of the total contact force at the luminal surface of the artery after stent implantation, and can in some sense be related to extent of tissue prolapse through the stent cells. D_2 is a measure of the change in maximum principal Cauchy stress within the artery wall between physiological conditions without stenting and physiological conditions after stenting. LG is the measure of luminal gain afforded by stent placement. The factory stent and the stent with fewer struts gave luminal gains of 48% and 47%, respectively, compared to the 18% achieved through angioplasty damage only. The stent with thinner struts gave an LG of 42%. While the factory stent and the stent with fewer struts caused roughly equal stress changes within the wall, the latter stent caused significantly higher contact stresses at the luminal surface. This makes the stent with fewer struts more likely to damage the intimal surface, with no significant gain in lumen area over the factory stent. The authors noted that D_1 and D_2 were lowest for the stent with thinner struts, and its LG was not too far below that of the other stents, possibly indicating that thinner struts are preferred in avoiding vessel damage. This is in agreement with clinical studies that identified stents with thinner struts as causing less restenosis as determined angiographically [141, 142].

14   Current Developments

It is clear from the small sample of studies presented in this chapter that vascular mechanics research has made great progress in recent years. Advances in computation, constitutive modeling, fluid-structure interaction, medical imaging, and image

processing have allowed us to reach the point where detailed and accurate studies may be made of a *real* artery, healthy or not. Models are being used more and more to ferret out the complex interplay between mechanics and biology and simulations are helping us understand the natural progression of vascular diseases. Limitations of idealized geometries and simple but insufficient material formulations have given way to sophisticated simulations that are steadily progressing to the stage of routine clinical utility.

We are not quite there, however, and much work remains to be done before vascular mechanics simulations are accurate enough, robust enough, efficient enough, and specific enough to be used broadly in the staging of disease or in the design of a patient-specific therapy. The role of simulation to these ends is still limited to a few applications at a small number of research hospitals. In addition to the modeling challenges discussed here, many unanswered questions remain about how best to use the vast amount of data generated in modern simulations. Several mechanical descriptors have been correlated to the initiation, progression, and catastrophic resolutions of atherosclerotic and aneurysmal diseases, but there are still no universally accepted mechanical environments linked to these biological phenomena.

One of the biggest challenges in achieving this level of understanding and utility is the stark lack of constitutive modeling techniques that can accurately represent the tissues and plaque materials of a *specific* diseased vessel without direct mechanical testing. Additionally, methods to discern and then incorporate into simulation the residual stresses that may be present in a diseased vessel are also lacking. Recent work in elastography shows promise that we will be able to discern patient-specific material properties, at least within some restricted range of loading conditions. In elastography, medical imaging data from MRI, OCT, or IVUS is used to establish a strain map for the arterial tissue. This is typically done by calculating a cross-correlation of data frames captured at different known pressure loads. In the transverse approach most often employed, image resolution, noise, and out of plane motion are deleterious to the accuracy of the strain mapping. When a strain map is established, and the pressure load is known, the inverse problem is solved for material stiffness throughout the domain. Various methods are being explored for strain mapping and the solution of the inverse problem, and the reader is referred to [143–150] for a review of modern techniques.

As shown in several histological studies of atherosclerotic lesions, the inflammatory state of the plaque is an important determinant of its progression and rupture potential. Recently, contrast agents and imaging techniques have been developed so that MR imaging of plaque inflammation is possible. While such contrast agents and imaging strategies are not yet in standard clinical use worldwide, several studies have shown their efficacy and potential to compliment FEM studies of diseased vessels. Recent work by Tang and Howarth et al in [151–153] describes these methods, and the possible correlation of mechanical stress and inflammation in atheromatous plaques. The results of this work could have wide ranging implications on FEM simulations of atherosclerotic vessels, from correlative studies to region-specific material properties or stress interpretations.

Perhaps one of the more exciting developments in computational vascular mechanics is the trend toward incorporating "biochemomechanical" interactions into numerical simulations. To do this accurately, the biological response of arteries to mechanical and chemical stimuli like shear and hoop stresses and vasoactive substances must be well characterized at the cell and tissue level, and the time scales and spatial extents of the response must be modeled numerically. This requires a theory of "small-on-large" that integrates the vastly different temporal and spatial scales. Such work, although in its infancy, shows great promise in investigating the initiation and progression of aneurysmal disease, atherosclerosis, cerebral vasospasm, and chronic hypertension, in addition to normal vessel development. Descriptions of this fluid-solid-growth approach used by several groups to model vascular systems and their constant remodeling can be found in [69, 154–165].

References

1. Rosamond, W., et al.: Heart disease and stroke statistics – 2007 update: A report from the American Heart Association Statistics Committee and Stroke Statistics Subcommittee. Circulation. **115**(5), e69–171 (2007)
2. Humphrey, J.D.: Cardiovascular Solid Mechanics: Cells, Tissues, and Organs, xvi, p. 757. Springer, New York (2002)
3. Gasser, T.C., Ogden, R.W., Holzapfel, G.A.: Hyperelastic modelling of arterial layers with distributed collagen fibre orientations. J. R. Soc. Interface. **3**(6), 15–35 (2006)
4. Finlay, H.M., McCullough, L., Canham, P.B.: Three-dimensional collagen organization of human brain arteries at different transmural pressures. J. Vasc. Res. **32**(5), 301–312 (1995)
5. Laflamme, K., et al.: Adventitia contribution in vascular tone: insights from adventitia-derived cells in a tissue-engineered human blood vessel. Faseb. J. **20**(8), 1245–1247 (2006)
6. Maiellaro, K., Taylor, W.R.: The role of the adventitia in vascular inflammation. Cardiovasc. Res. **75**(4), 640–648 (2007)
7. Davies, M.G., Fulton, G.J., Hagen, P.O.: Clinical biology of nitric oxide. Br. J. Surg. **82**(12), 1598–610 (1995)
8. Guyton, A.C.: Textbook of Medical Physiology, 5th edn., xxxvi, p. 1194. Saunders, Philadelphia, PA (1976)
9. Guyton, A.C.: Cardiovascular physiology. Butterworths, London (1974)
10. Womersley, J.R.: Oscillatory flow in arteries III. Flow and pulse-velocity formulae for a liquid whose viscosity varies with frequency. Phys. Med. Biol. **2**(4), 374–382 (1958)
11. Womersley, J.R.: Oscillatory flow in arteries II. The reflection of the pulse wave at junctions and rigid inserts in the arterial system. Phys. Med. Biol. **2**(4), 313–323 (1958)
12. Womersley, J.R.: Oscillatory flow in arteries: The constrained elastic tube as a model of arterial flow and pulse transmission. Phys. Med. Biol. **2**(2), 178–187 (1957)
13. Womersley, J.R.: Mathematical theory of oscillating flow in an elastic tube. J. Physiol. **127**(2), 37–8P (1955)
14. Morgan, G.W., Kiely, J.P.: Wave propagation in a viscous liquid contained in a flexible tube. Acoust. Soc. Am. **26**(3), 323–328 (1954)
15. Atabek, H.B., Lew, H.S.: Wave propagation through a viscous fluid contained in a tethered, initially stressed, orthotropic tube. Biophys. J. **8**, 626–649 (1968)
16. Atabek, H.B., Lew, H.S.: Wave propagation through a viscous incompressible fluid contained in an initially stressed elastic tube. Biophys. J. **6**, 481–503 (1966)
17. Vaishnav, R.N. and Vossoughi, J.: Estimation of residual strains in aortic segments. In: Hall, C.W. (ed.) Biomedical Engineering II, Recent Developments, vol. 2, pp. 330–333. Pergamon Press, New York, Oxford (1983)

18. Chuong, C.J., Fung, Y.C.: Three-dimensional stress distribution in arteries. J. Biomech. Eng. **105**(3), 268–274 (1983)
19. Delfino, A.: Analysis of Stress Field in a Model of the Human Carotid Bifurcation, in Physics, p. 106. Ecole Polytechnique Federale De Lausanne (1996)
20. Bergel, D.H.: The viscoelastic properties of the arterial wall. University of London (1960)
21. Holzapfel, G.A., Gasser, T.C., Ogden, R.W.: A new constitutive framework for arterial wall mechanics and a comparative study of material models. J. Elasticity. **61**, 1–48 (2000)
22. Takamizawa, K., Hayashi, K.: Strain energy density function and uniform strain hypothesis for arterial mechanics. J. Biomech. **20**(1), 7–17 (1987)
23. Hayashi, K., et al.: Stiffness and elastic behavior of human intracranial and extracranial arteries. J. Biomech. **13**(2), 175–84 (1980)
24. Hayashi, K., et al.: Mechanical properties of human cerebral arteries. Biorheology. **17**(3), 211–218 (1980)
25. Patel, D.J., Fry, D.L.: The elastic symmetry of arterial segments in dogs. Circ. Res. **24**(1), 1–8 (1969)
26. Carew, T.E., Vaishnav, R.N., Parel, D.J.: Compressibility of the arterial wall. Circ. Res. **23**, 61–69 (1968)
27. Bergel, D.H.: The dynamic elastic properties of the arterial wall. J Physiol (Lond.) **156**: 458–469 (1961)
28. Peterson, L.H., Jensen, R.E., Parnell, J.: Mechanical properties of arteries in vivo. Circ. Res. **8**, 622–639 (1960)
29. Zhang, W., Liu, Y., Kassab, G.S.: Viscoelasticity reduces the dynamic stresses and strains in the vessel wall: Implications for vessel fatigue. Am. J. Physiol. Heart. Circ. Physiol. **293**(4), H2355–2360 (2007)
30. Fung, Y.C., Fronek, K., Patitucci, P.: Pseudoelasticity of ateries and the choice of its mathematical expression. Am. J. Physiol. **237**, H620–631 (1979)
31. Holzapfel, G.A.: Nonlinear Solid Mechanics: A Continuum Approach For Engineering, xiv, p. 455. Wiley, Chichester, New York (2000)
32. Holzapfel, G.A., Weizsacker, H.W.: Biomechanical behavior of the arterial wall and its numerical characterization. Comput. Biol. Med. **28**(4), 377–392 (1998)
33. Humphrey, J.D., Na, S.: Elastodynamics and arterial wall stress. Ann. Biomed. Eng. **30**(4), 509–523 (2002)
34. Weizsacker, H.W., Pinto, J.G.: Isotropy and anisotropy of the arterial wall. J. Biomech. **21**(6), 477–487 (1988)
35. Brant, A.M., et al.: Biomechanics of the arterial wall under simulated flow conditions. J. Biomech. **21**(2), 107–113 (1988)
36. Kuchar, N.R., Ostrach, S.: A thick walled viscoelastic model for the mechanics of arteries. J. Biomech. **2**(4), 443–454 (1969)
37. Raghavan, M.L., et al.: Three-dimensional finite element analysis of residual stress in arteries. Ann. Biomed. Eng. **32**(2), 257–263 (2004)
38. von Maltzahn, W.W., Warriyar, R.G.: Experimental measurements of elastic properties of media and adventitia of bovine carotid arteries. J. Biomech. **17**(11), 839–847 (1984)
39. Chaudhry, H.R., et al.: Residual stresses in oscillating thoracic arteries reduce circumferential stresses and stress gradients. J. Biomech. **30**(1), 57–62 (1997)
40. Schulze-Bauer, C.A., Holzapfel, G.A.: Determination of constitutive equations for human arteries from clinical data. J. Biomech. **36**(2), 165–169 (2003)
41. Holzapfel, G.A., et al.: Large strain analysis of soft biological membranes: Formulation and finite element analysis. Comput. Meth. Appl. Mech. Eng. **132**, 45–61 (1996)
42. Vorp, D.A., et al.: Identification of elastic properties of homogeneous, orthotropic vascular segments in distension. J. Biomech. **28**(5), 501–512 (1995)
43. Chuong, C.J., Fung, Y.C.: Compressibility and constitutive equation of arterial wall in radial compression experiments. J. Biomech. **17**(1), 35–40 (1984)
44. Humphrey, J.D., et al.: Computer-aided vascular experimentation: A new electromechanical test system. Ann. Biomed. Eng. **21**(1), 33–43 (1993)

45. Walker, J.C., et al.: Magnetic resonance imaging-based finite element stress analysis after linear repair of left ventricular aneurysm. J Thorac Cardiovasc Surg. **135**(5): 1094–1102, 1102 e1–2 (2008)
46. Einstein, D.R., et al.: Inverse parameter fitting of biological tissues: A response surface approach. Ann. Biomed. Eng. **33**(12): 1819–1830 (2005)
47. Bathe, K.-J.: Finite element procedures., p. 1037. Prentice Hall xiv, Englewood Cliffs, NJ (1996)
48. Demiray, H.: A note on the elasticity of soft biological tissues. J. Biomech. **5**(3), 309–311 (1972)
49. Tang, D., et al.: Steady flow and wall compression in stenotic arteries: A three-dimensional thick-wall model with fluid-wall interactions. J. Biomech. Eng. **123**(6), 548–557 (2001)
50. Tang, D., et al.: Effect of a lipid pool on stress/strain distributions in stenotic arteries: 3-D fluid-structure interactions (FSI) models. J. Biomech. Eng. **126**(3), 363–370 (2004)
51. Tang, D., et al.: A negative correlation between human carotid atherosclerotic plaque progression and plaque wall stress: in vivo MRI-based 2D/3D FSI models. J. Biomech. **41**(4), 727–736 (2008)
52. Tang, D., et al.: Quantifying effects of plaque structure and material properties on stress distributions in human atherosclerotic plaques using 3D FSI models. J. Biomech. Eng. **127**(7), 1185–1194 (2005)
53. Tang, D., et al.: 3D MRI-based multicomponent FSI models for atherosclerotic plaques. Ann. Biomed. Eng. **32**(7), 947–960 (2004)
54. Chuong, C.J., Fung, Y.C.: On residual stresses in arteries. J. Biomech. Eng. **108**(2), 189–192 (1986)
55. Li, Z.-Y., et al.: Structural analysis and magnetic resonance imaging predict plaque vulnerability: A study comparing symptomatic and asymptomatic individuals. J. Vascular Surg. **45**, 768–775 (2007)
56. Zhang, W., Wang, C., Kassab, G.S.: The mathematical formulation of a generalized Hooke's law for blood vessels. Biomaterials. **28**(24), 3569–3578 (2007)
57. Wang, C., Zhang, W., Kassab, G.S.: The validation of a generalized Hooke's law for coronary arteries. Am. J. Physiol. Heart. Circ. Physiol. **294**, H66–73 (2007)
58. Holzapfel, G.A., Gasser, T.C., Ogden, R.W.: Comparison of a multi-layer structural model for arterial walls with a fung-type model, and issues of material stability. J. Biomech. Eng. **126**(2), 264–275 (2004)
59. Wuyts, F.L., et al.: Elastic properties of human aortas in relation to age and atherosclerosis: a structural model. Phys. Med. Biol. **40**(10), 1577–1597 (1995)
60. Holzapfel, G.A., Gasser, T.C.: A viscoelastic model for fiber-reinforced composites at finite strains: Continuum basis, computational aspects and applications. Comput. Meth. Appl. Mech. Eng. **190**, 4379–4403 (2001)
61. Gasser, T.C., Holzapfel, G.A.: A rate-independent elastoplastic constitutive model for biological fiber-reinforced composites at finite strains: Continuum basis, algorithmic formulation and finite element implementation. Comput. Mech. **29**, 340–360 (2002)
62. Holzapfel, G.A., et al.: Determination of layer-specific mechanical properties of human coronary arteries with nonatherosclerotic intimal thickening and related constitutive modeling. Am. J. Physiol. Heart. Circ. Physiol. **289**, H2048–2058 (2005)
63. Kroon, M., Holzapfel, G.A.: A new constitutive model for multi-layered collagenous tissues. J. Biomech. **41**(12), 2766–2771 (2008)
64. Zulliger, M.A., et al.: A strain energy function for arteries accounting for wall composition and structure. J. Biomech. **37**, 989–1000 (2004)
65. Milnor, W.R.: Hemodynamics. Williams and Wilkins, Baltimore (1989)
66. Carton, R.W., Dainauskas, J., Clark, J.W.: Elastic properties of single elastic fibers. J Appl Physiol. **17**, 547–551 (1962)
67. Roy, S., et al.: On the in-series and in-parallel contribution of elastin assessed by a structure-based biomechanical model of the arterial wall. J. Biomech. **41**(4), 737–743 (2008)
68. Ogden, R.W., Saccomandi, G.: Introducing mesoscopic information into constitutive equations for arterial walls. Biomech. Model. Mechanobiol. **6**(5), 333–344 (2007)

69. Rachev, A., Hayashi, K.: Theoretical study of the effects of vascular smooth muscle contraction on strain and stress distributions in arteries. Ann. Biomed. Eng. **27**, 459–468 (1999)
70. Holzapfel, G.A., Gasser, T.C.: Computational stress-deformation analysis of arterial walls including high-pressure response. Int. J. Cardiol. **116**(1), 78–85 (2007)
71. Donea, J., et al.: Arbitrary Lagrangian-Eulerian methods. In: Stein, E., de Borst, R. and Hughes, T.J.R. (eds.) Encyclopedia of Computational Mechanics. Wiley, New York (2004)
72. Morand, H.J.P. and Ohayon, R.: Fluid Structure Interaction: Applied Numerical Methods. Wiley, New York (1995)
73. Rugonyi, S., Bathe, K.J.: On finite element analysis of fluid flows fully coupled with structural interactions. CMES: Comput. Model. Eng. Sci. **2**(2), 195–212 (2001)
74. Tang, D., et al.: Wall stress and strain analysis using a three-dimensional thick-wall model with fluid-structure interactions for blood flow in carotid arteries with stenoses. Comput. Struc. **72**, 341–356 (1999)
75. Tang, D., Yang, C., Ku, D.N.: A 3-D thin-wall model with fluid-structure interactions for blood flow in carotid arteries with symmetric and asymmetric stenoses. Comput. Struc. **72**, 357–377 (1999)
76. Tang, D., et al.: A nonlinear axisymmetric model with fluid-wall interactions for steady viscous flow in stenotic elastic tubes. J. Biomech. Eng. **121**(5), 494–501 (1999)
77. Tang, D., et al.: Effect of stenosis asymmetry on blood flow and artery compression: A three-dimensional fluid-structure interaction model. Ann. Biomed. Eng. **31**, 1182–1193 (2003)
78. Hafner, C.D.: Minimizing the risks of carotid endarterectomy. J. Vasc. Surg. **1**(3), 392–397 (1984)
79. Ku, D.N., et al.: A new hydrogel for soft tissue engineering application, in Biomedical engineering society 1997 annual fall meeting. San Diego, CA (1997)
80. Perktold, K., Rappitsch, G.: Computer simulation of local blood flow and vessel mechanics in a compliant carotid artery bifurcation model. J. Biomech. **28**(7), 845–856 (1995)
81. Ku, D.N., et al.: Pulsatile flow and atherosclerosis in the human carotid bifurcation. Positive correlation between plaque location and low oscillating shear stress. Arteriosclerosis. **5**(3), 293–302 (1985)
82. Salzar, R.S., Thubrikar, M.J., Eppink, R.T.: Pressure-induced mechanical stress in the carotid artery bifurcation: a possible correlation to atherosclerosis. J. Biomech. **28**(11), 1333–1340 (1995)
83. Fung, Y.C.: Biomechanics – mechanical properties of living tissues, pp. 261–296. Springer, New York (1981)
84. Delfino, A., et al.: Residual strain effects on the stress field in a thick wall finite element model of the human carotid bifurcation. J. Biomech. **30**(8), 777–786 (1997)
85. Bharadvej, B.K., Mabon, W.F., Giddens, D.P.: Steady flow in a model of a human carotid bifurcation. J. Biomech. **15**, 349–362 (1982)
86. Younis, H.F., et al.: Computational analysis of the effects of exercise on hemodynamics in the carotid bifurcation. Ann. Biomed. Eng. **31**(8), 995–1006 (2003)
87. Hariton, I., et al.: Stress-driven collagen fiber remodeling in arterial walls. Biomech. Model. Mechanobiol. **6**(3), 163–175 (2007)
88. Dammert, S., et al.: Detection of intracranial aneurysms with multislice CT: comparison with conventional angiography. Neuroradiology. **46**(6), 427–434 (2004)
89. Lell, M.M., et al.: New techniques in CT angiography. Radiographics. **26**(Suppl 1), S45–62 (2006)
90. Saloner, D.A.: Magnetic Resonance Angiography, in MRI and CT of the Cardiovascular System, In Higgins, C.B. and de Roos, A. (eds.) Lippincot Williams & Wilkins, Philadelphia, PA (2006)
91. Gullberg, G.T., et al.: MR vascular imaging with a fast gradient refocusing pulse sequence and reformatted images from transaxial sections. Radiology. **165**(1), 241–246 (1987)
92. Parker, D.L., Yuan, C., Blatter, D.D.: MR angiography by multiple thin slab 3D acquisition. Magn. Reson. Med. **17**(2), 434–451 (1991)
93. Dumoulin, C.L., et al.: Three-dimensional phase contrast angiography. Magn. Reson. Med. **9**(1), 139–149 (1989)

94. Saloner, D.: Determinants of image appearance in contrast-enhanced magnetic resonance angiography. A review. Invest. Radiol. **33**(9), 488–495 (1998)

95. Zhang, S., et al.: Comparison of carotid vessel wall area measurements using three different contrast-weighted black blood MR imaging techniques. Magn. Reson. Imaging. **19**(6), 795–802 (2001)

96. Zhao, S.Z., et al.: Blood flow and vessel mechanics in a physiologically realistic model of a human carotid arterial bifurcation. J. Biomech. **33**(8), 975–984 (2000)

97. Zhao, S.Z., et al.: Inter-individual variations in wall shear stress and mechanical stress distributions at the carotid artery bifurcation of healthy humans. J. Biomech. **35**(10), 1367–1377 (2002)

98. Younis, H.F., et al.: Hemodynamics and wall mechanics in human carotid bifurcation and its consequences for atherogenesis: Investigation of inter-individual variation. Biomech. Model. Mechanobiol. **3**(1), 17–32 (2004)

99. Kaazempur-Mofrad, M.R., et al.: Characterization of the atherosclerotic carotid bifurcation using MRI, finite element modeling, and histology. Ann. Biomed. Eng. **32**(7), 932–946 (2004)

100. Stoll, G., Bendszus, M.: Inflammation and atherosclerosis: Novel insights into plaque formation and destabilization. Stroke. **37**, 1923–1932 (2006)

101. Richardson, P.D.: Biomechanics of plaque rupture: Progress, problems, and new frontiers. Ann. Biomed. Eng. **30**, 524–536 (2002)

102. Forrester, J.S.: The pathogenesis of atherosclerosis and plaque instability: In: Holtzman, J.L. (ed.) Atherosclerosis and Oxidant Stress: A New Perspective. Springer: New York (2007)

103. Loree, H.M., et al.: Effects of fibrous cap thickness on peak circumferential stress in model atherosclerotic vessels. Circ. Res. **71**, 850–858 (1992)

104. Imoto, K., et al.: Longitudinal structural determinants of atherosclerotic plaque vulnerability: a computational analysis of stress distribution using vessel models and three-dimensional intravascular ultrasound imaging. J. Am. Coll. Cardiol. **46**(8), 1507–1515 (2005)

105. Li, Z.Y., et al.: How critical is fibrous cap thickness to carotid plaque stability? A flow-plaque interaction model. Stroke. **37**(5), 1195–1199 (2006)

106. Lendon, C.L., et al.: Atherosclerotic plaque caps are locally weakened when macrophage density is increased. Atherosclerosis. **87**, 87–90 (1991)

107. Huang, H., et al.: The impact of calcification on the biomechanical stability of atherosclerotic plaques. Circulation. **103**, 1051–1056 (2001)

108. Vengrenyuk, Y., et al.: A hypothesis for vulnerable plaque rupture due to stress-induced debonding around cellular microcalcifications in thin fibrous caps. Proc. Natl. Acad. Sci. USA. **103**(40), 14678–14683 (2006)

109. Avrahami, I., et al.: Influence of microcalcifications in thin-cap fibroatheroma of a vulnerable plaque using FEM-FSI model. in BIO2006. ASME, Amelia Island, Florida, USA (2006)

110. Bluestein, D., et al.: Influence of microcalcifications on vulnerable plaque mechanics using FSI modeling. J. Biomech. **41**, 1111–1118 (2008)

111. Versluis, A., Bank, A.J., Douglas, W.H.: Fatigue and plaque rupture in myocardial infarction. J. Biomech. **39**, 339–347 (2006)

112. Cheng, G.C., et al.: Distribution of circumferential stress in ruptured and stable atherosclerotic lesions. A structural analysis with histopathological correlation. Circulation. **87**(4), 1179–1187 (1993)

113. Kaazempur-Mofrad, M.R., et al.: Cyclic strain in human carotid bifurcation and its potential correlation to atherogenesis: Idealized and anatomically-realistic models. J. Eng. Math. **47**, 299–314 (2003)

114. Patel, S.Y., et al.: In: 2003 Summer Bioengineering Conference. Sonesta Beach Resort in Key Biscayne, Florida (2003)

115. Ohayon, J., et al.: Influence of residual stress/strain on the biomechanical stability of vulnerable coronary plaques: Potential impact for evaluating the risk of plaque rupture. Am. J. Physiol. Heart. Circ. Physiol. **293**(3), H1987–1996 (2007)

116. Chau, A.H., et al.: Mechanical analysis of atherosclerotic plaques based on optical coherence tomography. Ann. Biomed. Eng. **32**(11), 1494–1503 (2004)

117. Li, Z.Y., et al.: Stress analysis of carotid plaque rupture based on in vivo high resolution MRI. J. Biomech. **39**(14), 2611–2622 (2006)
118. Trivedi, R.A., et al.: Multi-sequence in vivo MRI can quantify fibrous cap and lipid core components in human carotid atherosclerotic plaques. Eur. J. Vasc. Endovasc. Surg. **28**(2), 207–213 (2004)
119. Trivedi, R.A., et al.: MRI-derived measurements of fibrous-cap and lipid-core thickness: The potential for identifying vulnerable carotid plaques in vivo. Neuroradiology. **46**(9), 738–743 (2004)
120. Lovett, J.K., Rothwell, P.M.: Site of carotid plaque ulceration in relation to direction of blood flow: An angiographic and pathological study. Cerebrovasc. Dis. **16**(4), 369–375 (2003)
121. Kock, S.A., et al.: Mechanical stresses in carotid plaques using MRI-based fluid-structure interaction models. J. Biomech. **41**(8), 1651–1658 (2008)
122. Kock, S.A., et al.: Stresses in carotid plaques using MRI-based fluid structure interaction models. In: Nordic COMSOL Conference, Copenhagen, Denmark (2006)
123. Tang, D., et al.: Local maximal stress hypothesis and computational plaque vulnerability index for atherosclerotic plaque assessment. Ann. Biomed. Eng. **33**(12), 1789–801 (2005)
124. Yang, C., et al.: In-vivo/ex vivo MRI-based 3D models with fluid-structure interactions for human atherosclerotic plaques compared with fluid/wall-only models. CMES: Comput. Model. Eng. Sci. **19**(3), 710–719 (2007)
125. Holzapfel, G.A., Stadler, M., Schulze-Bauer, C.A.: A layer-specific three-dimensional model for the simulation of balloon angioplasty using magnetic resonance imaging and mechanical testing. Ann. Biomed. Eng. **30**(6), 753–767 (2002)
126. Gasser, T.C., Holzapfel, G.A.: Finite element modeling of balloon angioplasty by considering overstretch of remnant non-diseased tissues in lesions. Comput. Mech. 40, 47–60 (2007)
127. Gasser, T.C., Holzapfel, G.A.: Modeling plaque fissuring and dissection during balloon angioplasty intervention. Ann. Biomed. Eng. **35**(5), 711–723 (2007)
128. Sommer, G., et al.: Dissection properties of the human aortic media: an experimental study. J. Biomech. Eng. **130**(2), 021007 (2008)
129. Gasser, T.C., Holzapfel, G.A.: Modeling the propagation of arterial dissection. Eur. J. Mech. A/Solids. **25**, 617–633 (2006)
130. Auer, M., et al.: 3-D reconstruction of tissue components for atherosclerotic human arteries using ex vivo high-resolution MRI. IEEE Trans. Med. Imaging. **25**(3), 345–357 (2006)
131. Ferrara, A. and Pandolfi, A.: Numerical simulation of arterial plaque ruptures. Int J Mater Form (2008)
132. Ferrara, A., Pandolfi, A.: Numerical modelling of fracture in human arteries. Comput. Meth. Biomech. Biomed. Eng. **11**, 553–567 (2008)
133. Holzapfel, G.A., Sommer, G.: Anisotropic mechanical properties of tissue components in human atherosclerotic plaques. J. Biomech. Eng. **126**, 657–665 (2004)
134. Haslach, H.W. Rupture mechanisms in circulatory system vascular tissue. In 5th World Congress of Biomechanics: Munich. Elsevier, Germany (2006)
135. Liang, D.K., et al.: Finite element analysis of the implantation of a balloon-expandable stent in a stenosed artery. Int. J. Cardiol. **104**(3), 314–318 (2005)
136. Lally, C., Dolan, F., Prendergast, P.J.: Cardiovascular stent design and vessel stresses: A finite element analysis. J. Biomech. **38**(8), 1574–1581 (2005)
137. Medtronic, DISTANCE trial: whitepaper reporting on the direct stenting with angiographic and clinical evaluation of the S7 (DISTANCE) trial. medtronic AVE. (2002)
138. Rutsch, W., et al.: Clinical and angiographic results with the NIR stent: First International NIR Endovascular Stent Study (FINESS-II). Int. J. Cardiovasc. Intervent. **3**(3), 143–151 (2000)
139. Kiousis, D.E., Gasser, T.C., Holzapfel, G.A.: A numerical model to study the interaction of vascular stents with human atherosclerotic lesions. Ann. Biomed. Eng. **35**(11), 1857–1869 (2007)
140. Kiousis, D.E., Gasser, T.C., Holzapfel, G.A.: Smooth contact strategies with emphasis on the modeling of balloon angioplasty with stenting. Int. J. Num. Eng. **75**, 826–855 (2008)
141. Kastrati, A., et al.: Intracoronary stenting and angiographic results: strut thickness effect on restenosis outcome (ISAR-STEREO) trial. Circulation. **103**(23), 2816–2821 (2001)

142. Pache, J., et al.: Intracoronary stenting and angiographic results: Strut thickness effect on restenosis outcome (ISAR-STEREO-2) trial. J. Am. Coll. Cardiol. **41**(8), 1283–1288 (2003)
143. de Korte, C.L., van der Steen, A.F.: Intravascular ultrasound elastography: An overview. Ultrasonics. **40**(1–8), 859–865 (2002)
144. de Korte, C.L., et al.: Vascular tissue characterisation with IVUS elastography. Ultrasonics. **38**(1–8), 387–390 (2000)
145. Baldewsing, R.A., et al.: Finite element modeling and intravascular ultrasound elastography of vulnerable plaques: Parameter variation. Ultrasonics. **42**(1–9), 723–729 (2004)
146. Baldewsing, R.A., et al.: Robustness of reconstructing the Young's modulus distribution of vulnerable atherosclerotic plaques using a parametric plaque model. Ultrasound Med. Biol. **31**(12), 1631–1645 (2005)
147. Baldewsing, R.A., et al.: Assessment of vulnerable plaque composition by matching the deformation of a parametric plaque model to measured plaque deformation. IEEE Trans. Med. Imaging. **24**(4), 514–528 (2005)
148. Ribbers, H., et al.: Noninvasive two-dimensional strain imaging of arteries: validation in phantoms and preliminary experience in carotid arteries in vivo. Ultrasound Med. Biol. **33**(4), 530–540 (2007)
149. Khalil, A.S., Bouma, B.E., Kaazempur, M.R.: Mofrad A combined FEM/genetic algorithm for vascular soft tissue elasticity estimation. Cardiovasc. Eng. **6**(3), 93–102 (2006)
150. Khalil, A.S., et al.: Tissue elasticity estimation with optical coherence elastography: Toward mechanical characterization of in vivo soft tissue. Ann. Biomed. Eng. **33**(11), 1631–1639 (2005)
151. Howarth, S., et al.: Correlation of macrophage location and plaque stress distribution using USPIO-enhanced MRI in a patient with symptomatic severe carotid stenosis: a new insight into risk stratification. Br. J. Neurosurg. **21**(4), 396–398 (2007)
152. Howarth, S.P., et al.: Utility of USPIO-enhanced MR imaging to identify inflammation and the fibrous cap: A comparison of symptomatic and asymptomatic individuals. Eur J Radiol. 2008 (in press)
153. Tang, T.Y., et al.: Correlation of carotid atheromatous plaque inflammation with biomechanical stress: utility of USPIO enhanced MR imaging and finite element analysis. Atherosclerosis. **196**(2), 879–887 (2008)
154. Kuhl, E., et al.: Computational modeling of arterial wall growth. Attempts towards patient-specific simulations based on computer tomography. Biomech. Model. Mechanobiol. **6**(5), 321–331 (2007)
155. Alastrue, V., Martinez, M.A., Doblare, M.: Modelling adaptive volumetric finite growth in patient-specific residually stressed arteries. J. Biomech. 41(8), 1773–1781 (2008)
156. Alford, P.W., Humphrey, J.D., Taber, L.A.: Growth and remodeling in a thick-walled artery model: Effects of spatial variations in wall constituents. Biomech. Model. Mechanobiol. **7**(4), 245–262 (2008)
157. Zhang, W., Kassab, G.S.: Remodeling of conduit arteries in hypertension and flow-overload obeys a minimum energy principle. J. Biomech. **41**(11), 2567–2570 (2008)
158. Criscione, J.C.: Kinematics framework optimized for deformation, growth, and remodeling in vascular organs. Biomech. Model. Mechanobiol. **7**(4), 285–293 (2008)
159. Rachev, A.: Theoretical study of the effect of stress-dependent remodeling on arterial geometry under hypertensive conditions. J. Biomech. **30**(8), 819–827 (1997)
160. Rachev, A., et al.: A model of stress-induced geometrical remodeling of vessel segments adjacent to stents and artery/graft anastomoses. J. Theor. Biol. **206**(3), 429–443 (2000)
161. Rachev, A., Stergiopulos, N., Meister, J.J.: Theoretical study of dynamics of arterial wall remodeling in response to changes in blood pressure. J. Biomech. **29**(5), 635–642 (1996)
162. Rodriguez, J., Goicolea, J.M., Gabaldon, F.: A volumetric model for growth of arterial walls with arbitrary geometry and loads. J. Biomech. **40**(5), 961–971 (2007)
163. Baek, S., Rajagopal, K.R., Humphrey, J.D.: A theoretical model of enlarging intracranial fusiform aneurysms. J. Biomech. Eng. **128**(1), 142–149 (2006)

164. Baek, S., Valentin, A., Humphrey, J.D.: Biochemomechanics of cerebral vasospasm and its resolution: II Constitutive relations and model simulations. Ann. Biomed. Eng. **35**(9), 1498–1509 (2007)
165. Humphrey, J.D., Baek, S., Niklason, L.E.: Biochemomechanics of cerebral vasospasm and its resolution: I A new hypothesis and theoretical framework. Ann. Biomed. Eng. **35**(9), 1485–1497 (2007)